

## RESEARCH ARTICLE

10.1002/2016MS000854

## Key Points:

- A new advanced subdaily stochastic weather generator (AWE-GEN-2d) is presented
- The model combines physical and stochastic approaches to simulate key climate variables at high spatial and temporal resolution
- It is relatively computationally efficient and allows the generation of multiple realizations accounting for natural climate variability

## Supporting Information:

- Supporting Information S1
- Movie S1

## Correspondence to:

N. Peleg,  
nadav.peleg@sccer-soe.ethz.ch

## Citation:

Peleg, N., S. Fatichi, A. Paschalis, P. Molnar, and P. Burlando (2017), An advanced stochastic weather generator for simulating 2-D high-resolution climate variables, *J. Adv. Model. Earth Syst.*, 9, 1595–1627, doi:10.1002/2016MS000854.

Received 4 NOV 2016

Accepted 7 JUN 2017

Accepted article online 19 JUN 2017

Published online 10 JUL 2017

© 2017. The Authors.

This is an open access article under the terms of the Creative Commons Attribution-NonCommercial-NoDerivs License, which permits use and distribution in any medium, provided the original work is properly cited, the use is non-commercial and no modifications or adaptations are made.

## An advanced stochastic weather generator for simulating 2-D high-resolution climate variables

Nadav Peleg<sup>1</sup> , Simone Fatichi<sup>1</sup> , Athanasios Paschalis<sup>2</sup> , Peter Molnar<sup>1</sup> , and Paolo Burlando<sup>1</sup>
<sup>1</sup>Institute of Environmental Engineering, Hydrology and Water Resources Management, ETH Zurich, Zürich, Switzerland,

<sup>2</sup>Faculty of Engineering and the Environment, University of Southampton, Southampton, UK

**Abstract** A new stochastic weather generator, **Advanced WEather GENERator** for a two-dimensional grid (AWE-GEN-2d) is presented. The model combines physical and stochastic approaches to simulate key meteorological variables at high spatial and temporal resolution: 2 km × 2 km and 5 min for precipitation and cloud cover and 100 m × 100 m and 1 h for near-surface air temperature, solar radiation, vapor pressure, atmospheric pressure, and near-surface wind. The model requires spatially distributed data for the calibration process, which can nowadays be obtained by remote sensing devices (weather radar and satellites), reanalysis data sets and ground stations. AWE-GEN-2d is parsimonious in terms of computational demand and therefore is particularly suitable for studies where exploring internal climatic variability at multiple spatial and temporal scales is fundamental. Applications of the model include models of environmental systems, such as hydrological and geomorphological models, where high-resolution spatial and temporal meteorological forcing is crucial. The weather generator was calibrated and validated for the Engelberg region, an area with complex topography in the Swiss Alps. Model test shows that the climate variables are generated by AWE-GEN-2d with a level of accuracy that is sufficient for many practical applications.

## 1. Introduction

Weather generators (WGs) are numerical tools designed to simulate synthetic time series of various meteorological variables of theoretically infinite length for a given climate and location based only on historical observations. Many WGs exist, with different methods to compute the meteorological variables (i.e., stochastic-statistical or physical-dynamical approaches) for different spatial and temporal resolutions [for extensive reviews see Fowler *et al.*, 2007; Semenov and Barrow, 1997; Wilks and Wilby, 1999].

WGs are mainly employed to extend short-record time series in order to represent the natural (stochastic) climate variability [e.g., Fatichi *et al.*, 2016]. They can be used to generate time series of climatic variables in ungauged locations if WG parameters are spatially transferable [e.g., Haberlandt *et al.*, 2008]. WGs are also applied for climate downscaling purposes and to fill missing data from recorded time series [e.g., Peleg *et al.*, 2015a; Schuol and Abbaspour, 2007]. These models have been extensively used in agricultural, hydrological, ecological, geomorphological, and energy-related impact studies. For example, WGs were used to quantify the sensitivity of crop productivity to climate variability in agricultural applications [Semenov and Porter, 1995; Semenov, 2006; Mavromatis and Hansen, 2001; Dubrovský *et al.*, 2004]. In hydrology, WGs were used to generate long time series of precipitation that are required for estimates of flood risk [Paschalis *et al.*, 2014; Wheeler *et al.*, 2005], for extreme rainfall analysis [Peleg *et al.*, 2017, 2016], for assessing the sensitivity of the hydrological regime to climate change [Peleg *et al.*, 2015a] and for evaluations of water resources [Fowler *et al.*, 2000]. In ecological studies, climate ensembles were generated to examine the effects of climate change on ecosystems [Schlabing *et al.*, 2014]. WGs were also used in long-term land management and erosion studies [Collins *et al.*, 2004; Francipane *et al.*, 2015; Tucker and Bras, 2000] and in estimating the impact of climate change on hydropower production [Fatichi *et al.*, 2015; Minville *et al.*, 2010; Park and Kim, 2014]. Additionally, WGs are often employed for the downscaling of climate variables from global and regional scales to local scales [e.g., Caracciolo *et al.*, 2014; Fatichi *et al.*, 2013; Kim and Ivanov, 2015] and were recently used to partition different sources of uncertainty in climate change projections [Fatichi *et al.*, 2016].

Most of the WGs are using stochastic-statistical approaches based on reproducing statistical properties and correlations among climate variables that are derived from observed data. The first published WGs used a

simple first-order Markov chain model to generate daily rainfall occurrence [LeCam, 1961; Gabriel and Neumann, 1962]. A very popular stochastic WG was presented by Richardson [1981] [Wilks and Wilby, 1999] and WGs that were designed following it are known as “Richardson type WG.” Those WGs first produced a time series of wet-dry spells, then generated rainfall intensity for the wet periods and finally generated the other climate variables that are cross-correlated with the wet-dry sequence (the original model consists only of temperature and solar radiation). The “Richardson type WG” were later developed to include additional climate variables (e.g., daily wind speed and dew point) [see Parlange and Katz, 2000]. To-date, a number of subsequent WGs can be listed in the category of stochastic-statistical approaches, such as WGEN [Richardson and Wright, 1984], WXGEN [Sharpley and Williams, 1990], CLIGEN [Nicks et al., 1995], LARS-WG [Racsko et al., 1991; Semenov and Barrow, 1997, 2002], ClimGen [McKague et al., 2003], Met&Roll [Dubrovský et al., 2004], MOFRBC [Bardossy and Plate, 1992; Wetterhall et al., 2008], WeatherMan [Pickering et al., 1994], MarkSim [Jones and Thornton, 2000], AAFC-WG [Hayhoe, 2000; Qian et al., 2004], WM2 [Hansen and Mavromatis, 2001], and the WG used by the UK Met Office (UKCP09) [see Jones et al., 2009]. These WGs are station-scale generators, with time scales that range from daily (or hourly for precipitation) to annual, with daily resolution being the most common one.

An alternative approach to the use of WGs is to solve the physics of the climate system, i.e., to directly apply dynamic meteorological models that solve the nonlinear partial differential equations governing the dynamics and thermodynamics of the atmosphere. Climate or meteorological models (e.g., WRF [Skamarock et al., 2005] and COSMO-CLM [Rockel et al., 2008]) are not WGs but can be theoretically used to address the same type of problems. While being attractive and more physically sound, direct use of meteorological models has a fundamental limitation related to the computational constraints of running multiple realizations. For this reason, the approach has been mainly used for weather forecasting or to analyze specific climatic patterns rather than to explore internal climate variability. Only recently, climate models have started generating a large number of realizations [e.g., Deser et al., 2012; Thompson et al., 2015], but still at coarse spatial and temporal scales. A promising direction is the future development of an atmospheric model of intermediate complexity that will be able to dynamically generate key climate variables at a reduced computational cost [Gutmann et al., 2016].

A third way is represented by the combined use of stochastic-statistical and physical-dynamical methods. This hybrid approach adopts stochastic models using some essential description of the underlying physical process, e.g., the cloudiness effect on temperature variability or the dependency between vapor pressure deficit and temperature (strong correlation) or between temperature and shortwave incoming radiation (weaker and lagged correlation). This approach was implemented by Ivanov et al. [2007], based on the methodology of Curtis and Eagleson [1982]. Fatichi et al. [2011] added further improvements to the model presented by Ivanov et al. [2007], which led to the first version of the Advanced Weather Generator (AWE-GEN) model. AWE-GEN is an hourly WG capable of reproducing low-frequency and high-frequency characteristics of key climate variables (e.g., precipitation, temperature, cloud cover, shortwave radiation, vapor pressure, wind speed, and atmospheric pressure) for a single station.

Most of the existing WGs are designed for station-scale applications, or sometimes as multistation generators [Wilks and Wilby, 1999]. However, high spatial and temporal resolution climate data are needed to provide more realistic forcing for local climate impact assessments [Kerr, 2011], especially when used to feed distributed hydrological models. For example, high-resolution precipitation data increase hydrodynamical model performance for small urban catchments [Ochoa-Rodriguez et al., 2015] and enable better model prediction of sediment transport and deposition [Coulthard and Skinner, 2016] for medium size catchments. High-resolution temperature and incoming solar radiation data improve model prediction of crop yields [Hoffmann et al., 2015]. An ensemble of high-resolution climate data that represents the stochastic climate variability is therefore essential to properly estimate the uncertainty derived from the chaotic nature of climate, for instance, the uncertainty that propagates into reservoir levels [Fatichi et al., 2015] or stream flow prediction [Peleg et al., 2015a]. Ideally, high-resolution climate ensembles should be generated using physical models that solve the atmospheric dynamics. However, the high computational demand of these models [Prein et al., 2015] makes this alternative infeasible for many practical studies, which aim at investigating inherent climate variability, with typically available computational resources. Stochastic WGs are a suitable alternative to generate multiple realizations of climate variables at high spatial and temporal resolution in a reasonable time and with limited computational resources. Several methods were suggested for stochastic

simulations of gridded climate variables at daily or coarser resolution [e.g., *Hutchinson, 1995; Jones et al., 2009*]. However, to the best of our knowledge, grid-based stochastic WG simulating climate variables (beyond precipitation) at subdaily temporal resolution have not yet been presented.

In this manuscript, we introduce the AWE-GEN-2d (Advanced WEather GENerator for a two-dimensional grid) model that satisfies those two needs: (i) it is relatively parsimonious in terms of computations and allows the generation of multiple stochastic realizations in a fast and efficient way and (ii) it simulates the key climate variables (e.g., precipitation, cloud cover, shortwave radiation, air temperature, vapor pressure, relative humidity, wind speed, and atmospheric pressure) at high spatial and temporal resolution for a distributed domain in a gridded form. The model is suitable for studying the impacts of stochastic climate variability, spatial heterogeneity and temporal and spatial resolutions of climate forcing, as well as for climate downscaling. Its characteristics can be important for hydrological, ecological, agricultural, and geomorphological impact studies. The model can also be used in the context of climate change. This can be achieved by modifying the model parameters using climate data derived from dynamical climate models (i.e., GCMs and RCMs); however, this aspect is not addressed here. AWE-GEN-2d is a substantial evolution and combination of four preceding models: (i) AWE-GEN model [*Curtis and Eagleson, 1982; Ivanov et al., 2007; Fatichi et al., 2011*]; (ii) STREAP model [*Paschalis et al., 2013*]; (iii) HiReS-WG model [*Peleg and Morin, 2014*]; and (iv)

WINDS model [*Burlando et al., 2007*].

The WG structure is presented in the following sections together with an example where the model is calibrated and tested: the Engelberg region, an area of complex topography located in the Swiss Alps.

## 2. AWE-GEN-2d Structure

AWE-GEN-2d is composed of eight modules used to generate different variables: (i) precipitation and cloud cover fields; (ii) advection; (iii) near-surface air temperature field; (iv) atmospheric pressure field; (v) radiation and vapor pressure fields; (vi) relative humidity field; (vii) dew point temperature field; and (viii) near-surface wind speed field. The use of a combined stochastic-physically based weather generator allows us to implement certain physical relationships that cannot be easily described empirically. This is mostly important at the subdaily scales where the statistical correlations between meteorological variables are complex to model. The dependency between meteorological variables as implemented in the model is illustrated in Figure 1. For example, precipitation and cloudiness are generated through a joint stochastic process, cloud cover controls the incoming solar radiation and near-surface air temperature. In turn, solar radiation and air temperature influence vapor pressure (as a correlation exists

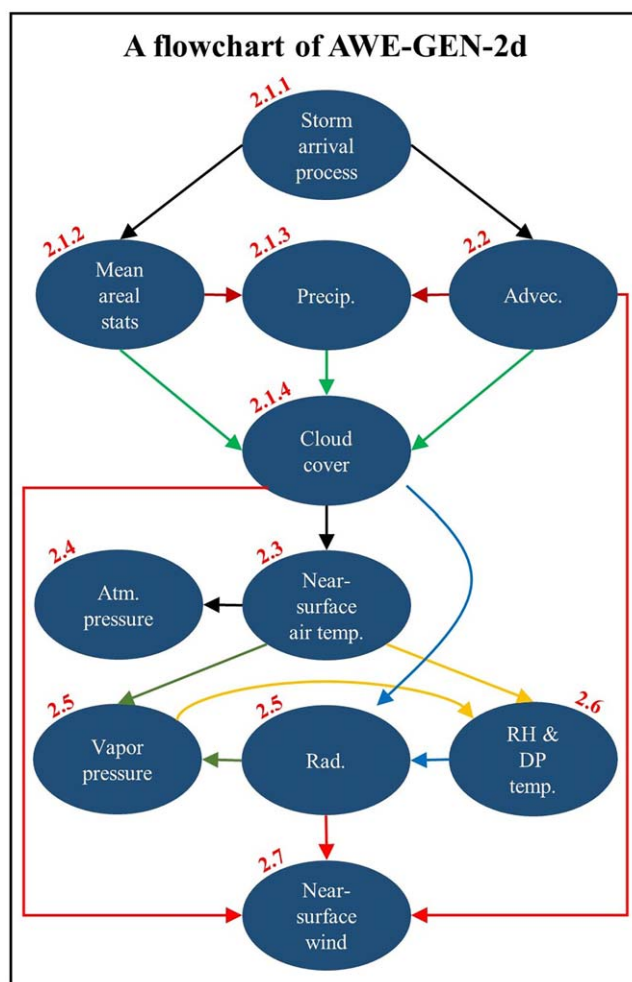


**Figure 1.** A schematic flowchart of AWE-GEN-2d, illustrating the relations between the simulated variables. Abbreviations: precip., precipitation; advec., advection; atm., atmospheric; temp., temperature; rad., radiation; RH, relative humidity; and DP, dew point. Topography directly affected all variables indicated below the cloud cover. Red numbers point to the relevant section where the variable is discussed in the main text.

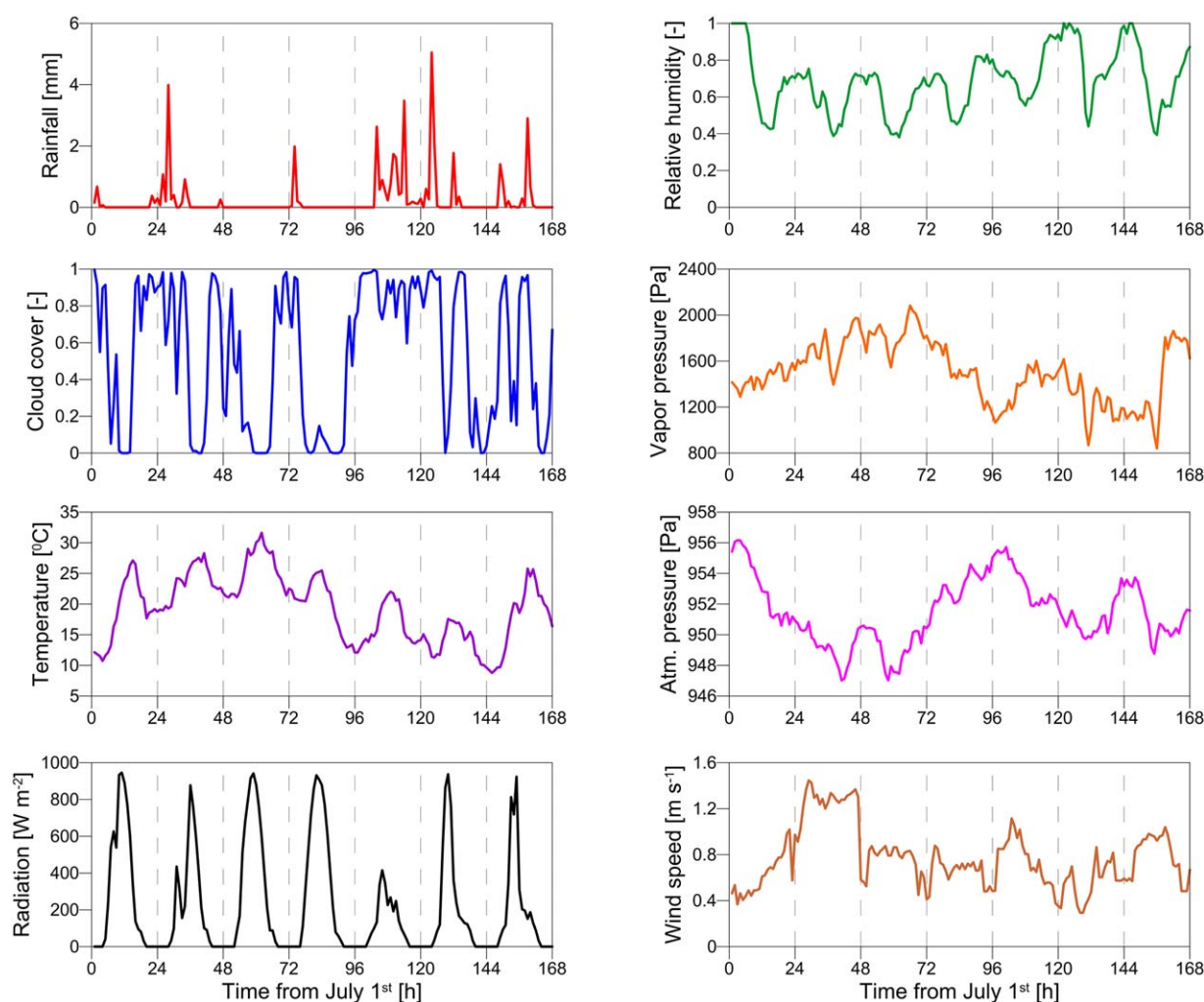


**Figure 2.** Simulated hourly values of climate variables with AWE-GEN-2d: precipitation, mean cloud cover in the areal domain, near-surface air temperature, incoming shortwave radiation, vapor pressure, relative humidity, atmospheric pressure, and near-surface wind speed. One random week is presented for one random cell (except mean areal cloud cover, which represents the entire domain), simulation start at midnight of the 1 July.

between global shortwave radiation at lag 1 and 2 h and vapor pressure deficit), and last, the cloudiness and solar radiation affect near-surface wind speed (through the empirical Pasquill stability cases). A qualitative example illustrating the interdependencies between different simulated variables is shown in Figure 2; the most rainy day in this example (between 96 and 120 h from the beginning of the simulation) is characterized by high cloud cover over the spatial domain, low near-surface temperature, higher relative humidity and low incoming shortwave radiation in comparison to the previous and following days (Figure 2).

The input to AWE-GEN-2d includes time series from ground stations (e.g., near-surface temperature), gridded data from remote sensing (precipitation) and areal averaged data from reanalysis products (cloud cover). Often, more than one source of data can/must be used per variable. A complete list of data input requires to AWE-GEN-2d is given in Table 1. The calibration of the different climate variables and model components is explained in detail in the supporting information (*Technical Reference*). The model parameters are listed in Table 2. For any given location it is expected that some modifications to the calibration procedure will be necessary as a result of differences in data availability. This can be the case when data have a different spatial or temporal resolution in comparison to the default resolution of the model, when the length of the data is too short for computing certain statistics or when the radar precipitation product is of low quality.

A description of each module is given in the following subsections. Detailed information about the stochastic and deterministic components and the corresponding equations are given in the *Technical Reference*



Table 1. List of Inputs to AWE-GEN-2d<sup>a</sup>

Input	Symbol	Type	Source
Wet area ratio	<i>WAR</i>	Time series	1
Cloud area ratio	<i>CAR</i>	Time series	1, 2
Mean areal precipitation	<i>IMF</i>	Time series	1
Gridded precipitation data	<i>IF</i>	Field	1
Geostrophic/advection wind	<i>U<sub>a</sub>, V<sub>a</sub></i>	Time series	1, 2
Near-surface temperature	<i>T</i>	Time series	3
Incoming global shortwave radiation	<i>RSW</i>	Time series	3
Near-surface atmospheric pressure	<i>P</i>	Time series	3
Aerosol optical depth	<i>AOD</i>	Time series	3
Cloud liquid water path	<i>LWP</i>	Time series	1, 2
Scattering albedos	<i>ω<sub>λ1</sub>, ω<sub>λ2</sub></i>	Constant	1, 3, 4
Ozone amounts in the atmosphere	<i>u<sub>o</sub></i>	Constant	1, 3, 4
Nitrogen dioxide amounts in the atmosphere	<i>u<sub>n</sub></i>	Constant	1, 3, 4
Ground albedo	<i>ρ<sub>g</sub></i>	Constant	1, 3, 4
Land use map	<i>LU</i>	Field	
Digital elevation map	<i>DEM</i>	Field	

<sup>a</sup>Potential data sources: 1, remote sensing (weather radar and satellite); 2, reanalysis database; 3, ground stations; and 4, literature.

that represents the supporting information of this article. References to the relevant sections in the Technical Reference are annotated from here on with the initials TR (e.g., TR-2.1, section 2.1 in the supporting information).

2.1. Precipitation and Cloud Cover

Precipitation is a key variable required by most environmental models, particularly by hydrological, geomorphological, and agricultural studies. It is almost always the first variable that is simulated in weather generators [Wilks and Wilby, 1999], and as such, it is the primary variable imposing statistical dependencies between the other model variables. In AWE-GEN-2d, precipitation and cloud cover are simulated simultaneously and are the first in the cascade of modeling modules (see Figure1). State of the art rainfall genera-

tors (i.e., computer models that simulate space-time rainfall fields) already exist and are focusing on generating rainfall over grids, at a high spatial and temporal resolution [e.g., Niemi et al., 2016; Paschalis et al., 2013; Peleg and Morin, 2014]. The space-time stochastic precipitation engine that is used in AWE-GEN-2d is the STREAP model that was presented by Paschalis et al. [2013], which is based on the String of Beads model [Pegram and Clothier, 2001a] and the studies of Bell [1987], and Kundu and Bell [2003]. This model enables the generation of precipitation fields at a high spatial and temporal resolution based on observed radar precipitation. For example, using common C-band radar data as input for the model, rainfall fields can be generated in a resolution of 1–2 km in space and 3–5 min in time. The structure of the STREAP model

Table 2. Parameters Calibrated in AWE-GEN-2d<sup>a</sup>

Parameter	Description	Estimated From	Module
$GP(\kappa_w, \sigma_w, \theta_w), J(\gamma_w, \delta_w, \mu_w, \sigma_w), GP(\kappa_d, \sigma_d, \theta_d), J(\gamma_d, \delta_d, \mu_d, \sigma_d)$	Parameters of the distributions of dry and wet spell durations	<i>WAR, IMF</i>	I (TR-1.1)
$\alpha, \nu_W, \nu_I, \nu_C, \nu_{WI}, \nu_{WC}, \nu_{CI}, \rho_{WI}, \rho_{WC}, \rho_{CI}$	Parameters of the Whittle-Matérn function for the tri-variate <i>WAR-IMF-CAR</i> process	<i>WAR, IMF, CAR</i>	I (TR-1.2.2)
$\rho_C, \nu_C$	Parameters of the T-copula for the Gaussian process <i>WAR-IMF-CAR</i> for each storm	<i>WAR, IMF, CAR</i>	I (TR-1.2.2)
$J(\gamma_{war}, \delta_{war}, \mu_{war}, \sigma_{war})$	Parameters of the distributions of <i>WAR</i>	<i>WAR</i>	I (TR-1.2.2)
$MGGP(W_{imf}, \alpha_{imf}, \beta_{imf}, \kappa_{imf}, \sigma_{imf})$	Parameters of the distributions of <i>IMF</i>	<i>IMF</i>	I (TR-1.2.2)
$J(\gamma_{car}, \delta_{car}, \mu_{car}, \sigma_{car})$	Parameters of the distributions of <i>CAR</i>	<i>CAR</i>	I (TR-1.2.2)
$\alpha_g$	Precipitation spatial correlation length	<i>IF</i>	I (TR-1.3.1)
$\phi^p_i, \theta^p_g$	Parameters of the ARMA process for the temporal evolution of the precipitation field	<i>IF</i>	I (TR-1.3.2)
$CV_r$	The coefficient of variation of the spatially distributed rainfall	<i>IF</i>	I (TR-1.3.5)
$GP(\kappa_o, \sigma_o, \theta_o), GP(\kappa_s, \sigma_s, \theta_s)$	Parameters of the Generalized Pareto distribution for the filter of the precipitation intensity field	<i>IF</i>	I (TR-1.3.6)
$a_{in}, b_{in}, c_{in}, d_{in}$	Parameters of the exponential coefficient for the cloud cover during interstorm	<i>CAR</i>	I (TR-1.4)
$\phi^c_i, \theta^c_g$	Parameters of the ARMA process for the temporal evolution of cloud cover during interstorm	<i>CAR</i>	I (TR-1.4)
$A^0_u, A^0_v, A^i_{uv}, A^i_{vu}, A^i_{uu}, A^i_{vv}, \epsilon_u, \epsilon_v$	Parameters of the bi-variate vector autoregressive model for the advection	<i>u, v</i>	II (TR-2)
$b_0, b_1, b_2, b_3, b_4$	Parameters of the deterministic temperature component	<i>T, CAR</i>	III (TR-3.1)
$d\overline{T}_{rh}, \rho_{dT}, \sigma_{dT,h}$	Parameters of the stochastic temperature component	<i>T</i>	III (TR-3.1)
$\gamma_T, \mu_{T_o,h}, \mu_{T_b,h}, \sigma_{T,h}$	Parameters for the temperature lapse rate	<i>T, DEM</i>	III (TR-3.2)
$\rho_{T,h}, \mu_{T,h}, \sigma_{T,h}, \mu_{T_o}, \sigma_{T_o}$	Parameters of the thermal inversion lapse rate	<i>T, DEM</i>	III (TR-3.3)
$\mu_{p_{o,m}}, \sigma_{p_{o,m}}, \rho_{p_{o,m}}$	Parameters for the AR process for the temporal evolution of atmospheric pressure	<i>P</i>	IV (TR-7)
$u_o, u_n, \omega_{\lambda 1}, \omega_{\lambda 2}, \rho_g$	Parameters for the clear-sky radiation model	Remote sensing	V (TR-4.1)
$\alpha_\lambda, \beta_\lambda$	Ångström turbidity parameters	<i>AOD</i>	V (TR-4.1)
$H_\beta$	Aerosol optical depth elevation parameter	<i>DEM, β<sub>λ</sub></i>	V (TR-4.5)
$a_{0,a}, a_{0,b}, a_{1,a}, a_{1,b}, a_{2,a}, a_{2,b}, a_{2,c}, a_{2,d}, a_{3,a}, a_{3,b}$	Parameters of the deterministic vapor pressure deficit component	<i>RSW, T, DEM</i>	V (TR-5)
$d\Delta e, \sigma_{d\Delta e}, \rho_{d\Delta e}$	Parameters of the stochastic vapor pressure deficit component	<i>RSW, T, DEM</i>	V (TR-5)
$\eta, \gamma_s, \gamma_c$	Parameters of the topographic correction of the wind model	<i>DEM</i>	VIII (TR-6.5)
$w_1, w_2, w_3, w_4, w_5, w_6, w_7$	Parameters of the roughness length	<i>LU, DEM</i>	VIII (TR-6.6)

<sup>a</sup>Abbreviations: GP, Generalized Pareto distribution; J, Johnson distribution; and MGGP, Mixed Gamma Generalized Pareto distribution.

was imported in AWE-GEN-2d (TR-1); it is based on three stages that are summarized in the following subsections: (i) storm arrival; (ii) within-storm temporal evolution of areal precipitation properties; and (iii) temporal evolution of the two-dimensional storm structure.

### 2.1.1. Storm Arrival Process

The storm arrival process (TR-1.1) is represented by an alternating renewal process, which defines a temporal sequence of dry and wet periods in the spatial region of interest. The dry and wet spell durations are sampled from specific probability distributions and are mutually independent. Three probability distributions are fitted to the data on a monthly basis: a Generalized Pareto distribution [e.g., *Embrechts et al.*, 1997]; a Lognormal distribution [e.g., *Papoulis and Unnikrishna*, 2002]; and a Johnson distribution [Johnson, 1949]. The probability distribution that best represent each dry and wet period for each month is selected using a maximum likelihood estimation method.

### 2.1.2. Temporal Evolution of Storm Mean Areal Statistics

Each single continuously wet period is defined as a storm, i.e., a rain event that can possess stratiform (in general low rainfall intensity) to convective (mostly high rainfall intensity) characteristics (although the type of rainfall event cannot be explicitly forced). A storm does not necessarily imply that the entire region is covered by precipitation. Three variables describe the development of the areal statistics for each storm (TR-1.2): (i) the wet area ratio (*WAR*); (ii) the mean areal rainfall intensity (*IMF*); and (iii) the cloud area ratio (*CAR*). The *WAR* and *CAR* ratios range between 0 and 1, where 0 signifies no rain or clear-sky conditions and 1 is used to describe rainfall over the entire domain or complete overcast conditions, respectively. The three variables are autocorrelated and cross-correlated and thus have to be simulated as a tri-variate stochastic process. This was done by computing a Gaussian stochastic process with a covariance function belonging to the Whittle-Matérn class (following the *Parsimonious Multivariate Matérn Model* presented by *Gneiting* [2010]) for each storm. The calibration of the tri-variate *WAR-IMF-CAR* process (TR-1.2.2) is done on a monthly basis and is modeled in the frequency domain, using the fast computation algorithms of the fast Fourier transform (FFT) [see *Chambers*, 1995; *Frigo and Johnson*, 1998].

### 2.1.3. Spatiotemporal Evolution of the Storm Structure

The simulated *WAR* and *IMF* time series for each storm are transformed into the space-time evolution of the precipitation fields using latent Gaussian fields (TR-1.3 and *Paschalis et al.* [2013]). The spatial correlation of the Gaussian field depends only on the distance between the grid cells using a one-parameter exponential autocorrelation function (similar to *Bell* [1987]). A direct estimation of the spatial correlation function can be challenging due to typical data quality (e.g., clutter contamination of weather radar data) and therefore a tool to estimate the rainfall spatial correlation function is not hard-coded in AWE-GEN-2d model. However, examples of the calibration of the spatial precipitation fields were given by *Gutnisky and Josić* [2010], *Paschalis et al.* [2013], and *Peleg and Morin* [2014].

The spatial precipitation fields are also correlated in time by assuming that the Gaussian field in the Lagrangian system of coordinates can be described using an autoregressive moving average (ARMA) model. The parameters of the ARMA model are held constant for the entire simulation period (i.e., seasonality is not considered), due to the uncertainties involved in their estimation [*Paschalis et al.*, 2013]. For calibrating the temporal evolution of the precipitation field in the Lagrangian system of coordinates, we follow *Paschalis et al.* [2013], who proposed to estimate the average temporal autocorrelation function of the normalized precipitation fields using a constrained least squares fitting procedure matching the theoretical autocorrelation function of the ARMA process to the one of the data.

The two-dimensional Gaussian fields are simulated using the two-dimensional FFT method [*Lang and Potthoff*, 2011] taking into account the exponential decay of the spatial autocorrelation and the ARMA process (temporal correlation) for each time step. Due to the symmetries of the fast Fourier transform the generated fields can be folded, i.e., the field is treated as continuous between the east-west and south-north boundaries (see example in supporting information Figure S1). This property can be exploited to simulate advection of the fields in the Eulerian coordinate system (moving along the *u* and *v* components, see section 2.2) while preserving the spatial structure of the fields (TR-1.3.3). In order to avoid artifacts due to field symmetries, precipitation fields are simulated for a larger spatial extent (twice the domain size), while only the central area of the simulations is used.

In the original STREAP model, the probability of precipitation occurrence is equal across the domain. This is a key limitation for areas with strong orographic features, where the probability of precipitation occurrence

might be dependent on altitude [e.g., *Frei and Schär*, 1998], or along a coastline, where enhanced convective activity has been observed [e.g., *Peleg and Morin*, 2012]. Not many studies have focused on parametrizing spatial heterogeneity of precipitation fields in stochastic models [for a recent example see *Niemi et al.*, 2016]. *Paschalis* [2013] suggested a simple parametrization in order to include nonhomogeneity in STREAP, based on appropriate modifications of the simulated Gaussian fields [*Kleiber et al.*, 2012]. The idea is to add a filter on the simulated Gaussian field to generate regions in the domain where precipitation occurrence is more or less likely than average [*Paschalis*, 2013]. In AWE-GEN-2d, we apply a filter to modify the Gaussian fields and therefore precipitation occurrence on a seasonal basis (TR-1.3.4). After the correction is applied, the autocovariance function of the Gaussian field is not equal to the original Gaussian field that was simulated. This error is neglected here because typical differences lay within 1–5%.

The intermittent precipitation fields simulated using a Lognormal distribution need to be converted into a precipitation intensity field (TR-1.3.5). The variables required to transform the latent Gaussian field into a rainfall intensity field are the *IMF*, *WAR* (previously computed) and the rainfall spatial coefficient of variation (CV) in a given time step. The CV of the spatially distributed rainfall is assumed to be only dependent on the month and therefore it is the same for all storms of a month. It can be directly estimated from weather radar products [e.g., *Paschalis et al.*, 2013] or from a dense rain gauge network [e.g., *Peleg et al.*, 2016]. Note that using the same CV constrains the rainfall spatial variability for a given *IMF* and *WAR* to lower values than observed, i.e., the actual rainfall variability is likely underestimated. In the original STREAP model, the probability of precipitation intensity is equal across all the grid cells covering the domain. In AWE-GEN-2d, another filter is applied to adjust for variability in the rainfall intensity probability distribution for each grid cell based on observations (TR-1.3.6).

#### 2.1.4. Cloud Cover

In the original AWE-GEN model [*Ivanov et al.*, 2007; *Fatichi et al.*, 2011], the cloud cover, *CAR*, is considered to be a stochastic variable that has different dynamics during intrastorm and interstorm periods. During an intrastorm period, i.e., the hours with precipitation greater than zero, the value of cloudiness is assumed to be equal to 1. In AWE-GEN-2d, during the intrastorm period, the cloudiness and rainfall fields are cross-correlated and cloud cover has always an equal or larger extent than the precipitation field (section 2.1.2 and TR-1.2). During an interstorm period, the existence of a “fair weather” region is assumed [*Fatichi et al.*, 2011]. In general, during an interstorm period, the cloudiness decreases as a function of the time passed since the end of the previous storm and increases toward the beginning of the next storm. The mean *CAR* as a function of the temporal distance from a storm is described using a two term exponential function (TR-1.4). The stochastic component of the cloud cover series during an interstorm period is simulated through an autoregressive moving average ARMA model. The required parameters are fitted on a monthly basis to preserve the seasonality of cloudiness statistics.

During a storm, we assume that the spatial structure of the cloud cover is identical to the spatial structure of the precipitation given as input into the model. Therefore, the latent Gaussian fields are used for the generation of both precipitation and cloud fields (TR-1.5), meaning that the spatial and temporal correlation of the cloud field in the Lagrangian system is identical to the precipitation fields. The cloud field is made by Boolean values to represent cloud or no-cloud (1 or 0, respectively) for any given grid cell along the domain and for any given time. The latent Gaussian fields are also used for the generation of the cloud fields during intrastorm periods, assuming similarity of the cloud spatial correlation structure during storms and between storms.

#### 2.2. Advection

In AWE-GEN-2d, the precipitation and cloud fields are advected following a speed and direction vector at any given time step. The advection speed and direction are converted into a two-component vector along the Cartesian system of coordinates, *u* and *v*, where a positive *u* wind is from the west and a positive *v* wind is from the south. The stochastic component of the advection time series is simulated through a bi-variate vector autoregressive (VAR) model [e.g., *Lütkepohl*, 2005; *Neumaier and Schneider*, 2001; *Schneider and Neumaier*, 2001], which accounts for the temporal correlation structure between the *u* and *v* components (TR-2). The advection vectors are generated at the same temporal resolution as the rainfall fields.

The input required by the model (observed time series of the advection components *u* and *v*) can be estimated from weather radar data using tracking algorithms [e.g., *Kyznarov and Novk*, 2009; *Li et al.*, 1995; *Peleg*

and Morin, 2012]. Alternatively, it can be derived from reanalysis data, assuming advection is similar to the geostrophic wind or the wind at a specific reference level, e.g., wind at 500 hPa. The parameters of the VAR model are estimated using the maximum likelihood estimation method. Advection is analyzed on a monthly basis to preserve the seasonality of statistics and the analysis is performed both for wet periods (weather radar and reanalysis data can be used) and dry periods (reanalysis data only).

### 2.3. Near-Surface Air Temperature

The near-surface air temperature is simulated following a mixed physically based and stochastic approach that was developed by Curtis and Eagleson [1982] and later expanded by Ivanov *et al.* [2007] and Fatichi *et al.* [2011]. In the distributed domain, the air temperature is generated with an hourly time step first for a given reference level (e.g., mean sea level or mean elevation of the region). It is then spatially extrapolated to all grid cells using a variable, the stochastic lapse rate, which is also generated with an hourly time step. The spatial resolution of the near-surface temperature is a function of the resolution of the digital terrain model (DTM or DEM) that is used as input for AWE-GEN-2d. In order to maintain feasible computational times and preserve fine spatial features of the terrain, a grid cell resolution of 50–100 m is recommended. All other climate variables that will be subsequently generated (presented in the following subsections) share the same spatial and temporal (hourly) resolution of the air temperature field due to direct and indirect relations among them.

The generation of air temperature at a given reference level (TR-3.1) is simulated as the sum of a stochastic component and a deterministic component. The deterministic temperature component is assumed to be directly related to the underlying physical processes such as the divergence of radiative and heat fluxes. More specifically, the deterministic time-gradient of temperature is a function of the air temperature itself and of the incoming long-wave radiation, which is used to explain some of the differences in cooling between clear and cloudy nights [Ivanov *et al.*, 2007]. It is further related through two functions to the hourly position of the Sun and site geographic location [Curtis and Eagleson, 1982; Ivanov *et al.*, 2007; Fatichi *et al.*, 2011].

The stochastic temperature component is estimated through an autoregressive model AR(1). The random deviates of temperature exhibit a significant dependence on the hour of the day, which is accounted for in the model. The stochastic component is particularly important for the determination of extremes of air temperature. The coefficients and the parameters used to estimate the deterministic and stochastic components are evaluated on a monthly basis.

In AWE-GEN-2d, the air temperature at a given reference level can be generated with or without considering the shading effect of the terrain. If the domain is relatively flat and without a complex orography one might decide to neglect the terrain effect in order to speed up the computation time. If the topographic complexity of the terrain is important, then the shading effect for any grid cell and for any time step needs to be calculated. The shadow effect is calculated as a binary coefficient, which value is zero when the sloping surface is shadowed by neighboring terrain (i.e., when the horizon angle is lower than the zenith angle for a given solar azimuth), or equal to one when it is not shadowed [Dubayah and Loechel, 1997; Chen *et al.*, 2006]. No direct flux from the sun is reaching a shadowed point; yet, diffuse, direct-reflected and diffuse-reflected fluxes do [Dubayah and Loechel, 1997; Chen *et al.*, 2006]. A shading factor is then used to reduce the effect of the sun on the deterministic component of the temperature over the shaded cells.

The near-surface air temperature is calculated as the sum of the air temperature at reference level and a stochastic lapse rate (TR-3.2). A lapse rate is first generated for the entire domain (i.e., all grid cells are assigned to the same lapse rate) using a simple autoregressive model. The lapse rate for each of the grid cells is then linearly adjusted depending on the elevation distance of the cells from the reference level. The model parameters are defined on hourly and monthly basis, and are obtained from lapse rate statistics that are derived from ground stations.

AWE-GEN-2d enables the simulation of temperature cold pooling using a simple terrain analysis (TR-3.3). Cold-air pools are created during calm nights with clear-sky conditions (stable atmospheric conditions), as a result of radiative cooling at the surface that triggers a dense cold-air layer to flow down the slopes in deep and steep valleys [Whiteman, 1982; Price *et al.*, 2013; Frei, 2014]. If cold pools are present, two lapse rates are detected: (i) a positive lapse rate within the steep slopes along the valleys and the valleys themselves and



(ii) a negative lapse rate for the slopes above the steep areas and on the top of the mountains. There is no clear rule to separate between the two lapse rates and the profile between the lapse rates is also nonlinear [Chung *et al.*, 2006; Frej, 2014]. In AWE-GEN-2d, a reference layer is defined to distinguish between the two lapse rates where cold pooling takes place using a combination of curvature and flow accumulation indexes, in order to detect the deep-steep valleys in the domain. It is a rather simple modeling scheme, where other factors, e.g., land cover and topographic shading, are not considered. The occurrence of temperature cold pooling is correlated with the amplitude of the daily temperature cycle, as a high amplitude is often associated with calm, clear-sky conditions [Dai *et al.*, 1999]. In AWE-GEN-2d, lapse rate time series for the steep valley areas are stochastically generated following a distribution anamorphosis transformation [e.g., Schleiss *et al.*, 2009, 2012; Peleg *et al.*, 2016], which adjusts the stochastically generated lapse rate based on the observed correlation with the amplitude of the daily temperature cycle.

## 2.4. Atmospheric Pressure

The near-surface atmospheric pressure is generated as a time series using a simple autoregressive model AR(1) for a single reference level (i.e., a given elevation) and then extended to the entire domain taking into account the temperature and lapse rate values using the barometric equation (TR-7). The parameters of the model are estimated from the observed atmospheric pressure time series on a monthly basis using maximum likelihood.

## 2.5. Radiation and Vapor Pressure

Radiation and vapor pressure are simulated in the same module, as the vapor pressure is correlated with radiation (see below and in TR-4).

### 2.5.1. Radiation

In AWE-GEN-2d, the incoming shortwave radiation is calculated as in AWE-GEN [Fatichi *et al.*, 2011], with an extension for a two-dimensional grid. It is based on the atmospheric radiation transfer model *REST2* that was developed by Gueymard [2008] for clear-sky conditions. The parametrizations of Stephens [1978] and Slingo [1989] are used to compute transmittance for cloudy conditions. The clear-sky radiation component considers two bands: the ultraviolet/visible, *UV/VIS*, band with wavelengths [0.29–0.70  $\mu\text{m}$ ] and the near infrared, *NIR*, band with wavelengths [0.70–4.0  $\mu\text{m}$ ] [Gueymard, 2008].

The extraterrestrial radiation is partitioned in the fractions of 0.4651 in the *UV/VIS* band, and 0.5195 in the *NIR* band [Gueymard, 2008] and it can be obtained starting with the value of the solar constant  $1360.8 \text{ W m}^{-2}$ , as suggested by Kopp and Lean [2011]. This value is subsequently corrected to take into account for the ratio between the actual Earth-Sun distance and the mean Earth-Sun distance. The correction factor was derived by Iqbal [1983] as a function of the day of the year. Equations to calculate the instantaneous values of the solar altitude, solar azimuth, solar declination, sunrise local time, sunset local time, and daily length are also necessary and are mainly drawn from Eagleson [2002].

When extraterrestrial radiation enters the atmosphere it is attenuated by Rayleigh scattering, uniformly mixed gas absorption, ozone absorption, nitrogen dioxide absorption, water vapor absorption, and aerosol extinction [Gueymard, 1989, 2008]. The water vapor absorption is a function of the precipitable water in the atmospheric column, which is estimated from the dew point temperature using the empirical model of Iqbal [1983]. The equations to compute the direct and diffusive transmittance terms for both bands are given in Gueymard [2003, 2004, 2008] and in TR-4.1 and TR-4.2. The parameters required to compute the clear-sky radiation are the  $\text{O}_3$  and the  $\text{NO}_2$  amounts in the atmospheric column, the single scattering albedos, the surrounding ground albedo and the Ångström turbidity parameters from which the spectral aerosol optical depth (AOD) can be obtained through the Ångström equation. For a domain with a high elevation gradient, an exponential correction for the AOD is applied [after Ingold *et al.*, 2001].

Radiative properties of clouds are related to their type and structure and are mainly a function of the total vertical liquid water path (LWP), which remains almost constant for clouds with the same broadband optical thickness [Stephens, 1978]. Slingo [1989] simplified a multiband cloud transmittance model to include only four wavelength bands. The four band approach of Slingo [1989] is transferred into the two bands of Gueymard [2008]. The direct radiation for cloudy conditions is estimated as a linear combination of the fluxes from clear and cloudy fractions of the sky. The diffuse radiative fluxes for cloudy conditions result from the diffuse clear-sky fraction and from the direct radiation incident on the clouds and it is also estimated as a linear combination of the fluxes from clear and cloudy fractions of the sky. The backscattered

contribution under a cloudy sky is computed accounting for the effects of cloud transmittance. *Slingo* [1989] parametrization requires the cloud cover ratio and the cloud optical thickness, which is essential for the description of the radiative properties of clouds [Stephens, 1978]. The cloud optical thickness can be approximately parametrized in terms of the effective radius of cloud-droplet size distribution and LWP [Stephens, 1978]. The LWP for each hour is assumed to be a product of a monthly reference value of LWP and the ratio of cloudiness [Ivanov et al., 2007]. Detailed description of the parametrization is given in TR-4.3 and TR-4.4. By calibrating different reference LWPs for different months, this parametrization takes into account the average seasonal differences in cloud properties.

The spatial distribution of solar radiation over a domain is computed in AWE-GEN-2d as a function of the local topography and of the surrounding terrain through the sky view factor, shadow effect and terrain configuration factor [see Dozier and Frew, 1990; Dubayah and Loechel, 1997, TR-4.5]. The principal variable controlling incident radiation on a slope in mountainous terrain is the local solar illumination angle that is defined as the angle between the sun beam and the normal to the slope surface. The sky view factor describes the portion of the visible sky [Bonan, 2002] and in mountainous terrain the sky view factor can be obstructed by neighboring surfaces. Dozier and Frew [1990] provide a method to take this effect into account. It includes the possibility to account for a variable horizon angle surrounding the point of interest. Dozier and Frew [1990] derived also a terrain configuration factor, needed in the computation of reflected radiation, which approximates the total area between the point and the surrounding terrain for which the points are mutually visible. This simplification is motivated by the complexity in determining the geometric relationships between a particular location and all the surrounding terrain elements. As counterpart of sky view factor, the terrain configuration factor estimates the ratio of the surrounding terrain visible to the point and varies from 0 (only sky visible) to 1 (only terrain visible). The shadow effect is calculated as explained in section 2.3. The parameters required to evaluate the terrain effects on radiation, such as grid cell slope, aspect, and horizon angle for the various directions, are obtained from the analysis of the digital topography.

### 2.5.2. Vapor Pressure

In AWE-GEN-2d, the vapor pressure is computed in the same way as in the AWE-GEN model [Fatichi et al., 2011], but an extension is added to account for the differences in elevation of each grid cell in the domain. Similarly to the modeling of air temperature, vapor pressure is simulated using a combination of a deterministic and a stochastic component (TR-5). The atmospheric vapor pressure is calculated as the difference between the vapor pressure at saturation and the vapor pressure deficit, which is the modeled variable. The vapor pressure deficit shows a strong correlation with air temperature and a weaker correlation with global shortwave radiation lagged by several hours [Fatichi et al., 2011]. The deterministic component of vapor pressure deficit is related to air temperature through a cubic function and linearly to global shortwave radiation at lag 1 and 2 h. The deterministic coefficients change as a function of the elevation at any given grid cell in the domain. The stochastic component of vapor pressure deficit is modeled with an AR(1) approach and is also elevation dependent. The parameters of the deterministic component are estimated on a monthly basis using the least square approach comparing simulated vapor pressure deficit with locally observed vapor pressure deficit. The parameters of the stochastic component are evaluated using the time series of residuals after removing the deterministic component from the observed series.

### 2.6. Relative Humidity and Dew Point Temperature

The conversion of near-surface air temperature and vapor pressure to relative humidity and dew point temperature is mathematically straightforward. The relative humidity is computed by simply dividing the vapor pressure with the vapor pressure at saturation, which is calculated from the near-surface air temperature following Dingman [1994]. The dew point temperature is calculated based on the Magnus-Tetens equation [Roberts, 2010] taking into account the air temperature and relative humidity. Both calculations are computed for each grid cell and time step.

### 2.7. Near-Surface Wind Speed

The near-surface wind speed (e.g., 2 or 10 m above ground) is computed from the geostrophic wind speed, taking into account the Planetary Boundary Layer (PBL) height, cloud cover, and incoming solar radiation. The equations used in AWE-GEN-2d were taken from the WINDS (Wind-field Interpolation by Non-Divergent Schemes) model [Ratto et al., 1990, 1994; Georgieva et al., 2003; Burlando et al., 2007]. WINDS is a diagnostic

mass-consistent model for simulating three-dimensional wind fields in complex terrains at the mesoscale. WINDS is a further development of AIOLOS [Lalas, 1985; Lalas *et al.*, 1988] and NOABL models [Phillips, 1979]. The wind mass conservation component is not implemented in AWE-GEN-2d, which only uses the geostrophic drag law to compute the near-surface wind speed [Georgieva *et al.*, 2003]; in the following paragraphs a short description is provided (for further details see TR-6).

The speed and direction of the geostrophic wind, the atmospheric stability parameter and the roughness parameter are required as input to the model. The atmospheric stability is assumed to be the same for the whole domain, while the roughness parameter is different for each grid cell. The geostrophic wind is assumed to be identical to the simulated advection wind, it is applied to the entire domain and does not change with height (barotropic case).

The near-surface wind speed is calculated using the geostrophic drag law, which requires a simplified computation of the Monin-Obukhov length, the friction velocity per grid cell, and the PBL height. The near-surface wind speed can be computed only when all the above variables are calculated using the expressions that were provided for stable and neutral atmospheric conditions by Zilitinkevich [1989] and for unstable atmospheric condition by Ratto *et al.* [1990]. First, the atmospheric stability condition needs to be determined for each time step. The atmospheric stability is determined through the Pasquill stability classes (from extreme unstable to very stable atmospheric conditions) [see Pasquill, 1974], which are related to the Monin-Obukhov length as expressed by Liu and Goodin [1976]. The Pasquill stability class for each hour is determined based on the shortwave incoming solar radiation and the cloud cover following the scheme of Mohan and Siddiqui [1998]. In cases where more than one class can be considered, the near-surface wind speed is calculated for all possible classes and the atmospheric stability that best matches the conditions defined by Mohan and Siddiqui [1998] (supporting information Table S3) is chosen. The friction velocity is then calculated from the geostrophic drag law using an iterative procedure, which depends on the atmospheric stability itself [Georgieva *et al.*, 2003]. Finally, the PBL height is computed based on the equations given by Ratto *et al.* [1990] and Zilitinkevich [1989] for different atmospheric stabilities.

The simulated near-surface wind is adjusted according to the topographic slope and curvature to account for stronger winds at top of the mountains compared to the valley bottoms and weaker winds over slopes on leeward sides of mountains. This is accomplished by using the topographically driven wind correction suggested by Liston and Sturm [1998] and Liston and Elder [2006], which is not a part of the original WINDS model. The slope and curvature weights required by the methodology are assigned to be 0.5 (i.e., equal weighting) and no calibration method is employed in AWE-GEN-2d. Further details are given in TR-6.5.

The calculation suggested above for the near-surface wind speed is initialized using the geostrophic wind [following Georgieva *et al.*, 2003] which is required as a model input. However, in most cases the wind components of the geostrophic wind are unknown, and a time series of the wind components from a fixed geopotential height, e.g., 500 or 850 hPa, is used as model input instead. In this case the roughness length field needs to be calibrated to fit the wind at the near surface.

### 3. Case Study: Engelberg Region

AWE-GEN-2d skill was tested simulating the above mentioned climate variables and reproducing the climate for a given observed period. The input data used for the case study are given with the model (a built-in example), allowing a new user to experiment with the data requirements and model setup.

The Engelberg region, located in the Swiss Alps (Figure 3) (8.4°E, 46.8°N), was chosen for two main reasons: (i) it is characterized by complex orography, with elevation ranging between 404 and 3119 m above sea level, which meets our main goal of estimating the model performance in a complex terrain and (ii) it is well monitored, with five ground stations at different elevations located within 5 km distance from the catchment (Table 4).

#### 3.1. Data

A long record of climate variables, with 30 years of observations or more, is recommended in order to obtain climate statistics for a given period. For this case study, AWE-GEN-2d was set to simulate the current climate (from the 1980s to 2015). For some of the climate variables, e.g., subdaily rainfall measurements,

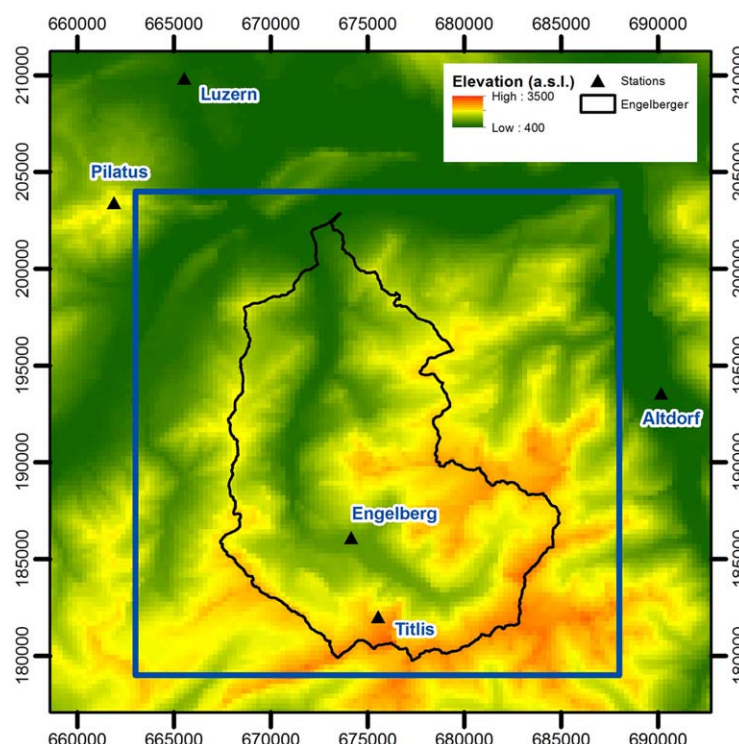


**Figure 3.** Digital elevation model of the Engelberg region. The simulated domain is delimited by a blue line. The hydrological catchment is bounded with a black line. Black triangles represent the five ground stations in and around the catchment. Coordinates are in the Swiss projection system (CH1903) and in meters.

long records are available for the entire period, while for others, e.g., subdaily radiation records, the observation period is shorter. An effort was made to obtain the longest record that represents the current climate for all the required variables, even if periods of data availability are not perfectly overlapping. The data used for setting and calibrating the model for the Engelberg region and their sources are summarized in Table 3.

Most of the data were supplied from the Swiss Federal Office for Meteorology and Climatology (MeteoSwiss) from three different products. High-resolution rainfall data (2 km and 5 min) for an 8 years period were obtained from MeteoSwiss weather radar system [Gabella *et al.*, 2005; Germann *et al.*, 2006].

Radar products passed qual-

ity checks and grid cells were additionally examined for substantial ground clutters or beam blockage.

Gridded 2 km daily rainfall estimates were derived from MeteoSwiss Grid-Data Product (RhiresD), which is based on an advanced two-stages spatial interpolation of daily precipitation totals measured with dense daily rain gauge network [Schwarb, 2000; MeteoSwiss, 2016] for a period of 32 years. Other MeteoSwiss Gridded-Products that were used are the TabsY [Frei, 2014], 2 km gridded data set of annual temperature (32 years), and SIS [Stöckli, 2013], 2 km gridded data set of annual global incoming shortwave radiation (9 years). TabsY is based on homogeneous measurement time series at multiple stations which are interpolated based on a regionalized nonlinear vertical temperature profile and a non-Euclidean “climatological” distance weighting of anomalies from the vertical profile [Frei, 2014]. SIS is based on the Heliosat algorithm [e.g., Hammer *et al.*, 2003], an empirical algorithm that correlates a satellite derived cloud index and the

Table 3. Summary of Data for the Case Study (MS = MeteoSwiss)				
Source	Spatial Resolution	Temporal Resolution	Period	Data
MS, rain gauges	Point	10 min	1983–2013	Storm duration (min)
MS, rain gauges	Point	10 min	1983–2013	Interstorm duration (min)
MS, ground-stations	Point	1 h	1984–2014	Temperature at station (°C)
MS, ground-stations	Point	1 h	1999–2015	Wind speed at 2m (m s <sup>−1</sup> )
MS, ground-stations	Point	1 h	2000–2014	Shortwave radiation (W m <sup>−2</sup> )
MS, ground-stations	Point	1 h	2004–2014	Atm. pressure at station (h Pa)
MS, ground-stations	Point	1 h	1985–2014	Vap. pressure at station (h Pa)
MS, Grid-Data	2 km	Daily	1981–2012	Rainfall intensity (mm d <sup>−1</sup> )
MS, Grid-Data	2 km	Annual	2004–2012	Shortwave radiation (W m <sup>−2</sup> )
MS, Grid-Data	2 km	Annual	1981–2012	Temperature at 2 m (°C)
MS, weather radar	2 km	5 min	2003–2010	Rainfall intensity (mm h <sup>−1</sup> )
Merra reanalysis	0.5° × 0.66°	1 h	1984–2014	Wind at 500 hPa (m s <sup>−1</sup> )
Merra reanalysis	0.5° × 0.66°	1 h	1984–2014	Cloud area ratio, CAR
AERONET	Point	15 min	2003–2014	Aerosol optical depth



**Table 4.** List of MeteoSwiss Ground Stations in the Engelberg Region

Name	Elevation (m)	Location
Altdorf	438	Valley
Engelberg	1036	Valley
Luzern	454	Lakeside
Pilatus	2106	Mountain top
Titlis	3040	Mountain top

radiation at the surface. SIS includes corrections for the effects of the terrain (e.g., shadowing and sky view) and an algorithm to distinguish between snow and clouds [Stöckli, 2013].

Station data were taken from MeteoSwiss SwissMetNet ground-stations surrounding the catchment (Figure 3 and Table 4). Station data for the following climate variables were extracted: precipitation (31 years of data), temperature (31 years), shortwave incoming radiation (15 years), vapor

pressure (30 years), atmospheric pressure (11 years), and wind speed (17 years). Data were recorded at 1 h temporal resolution, except for rainfall, which has a temporal resolution of 10 min.

The 500 hPa wind components and the cloud area cover were extracted for a 31 year period from the Merra reanalysis data set [Rienecker et al., 2011]. Merra grid size is approximately 50 km × 66 km in space and 1 h in time. Aerosol optical depth data (15 min temporal resolution from Laegeren ground-station) for a 12 year period were derived from the AERONET network [Holben et al., 2001].

The digital elevation model DHM25 (source: Swiss Federal Office of Topography) was used as topographic input for the model. It has a spatial resolution of 25 m and error of 2–8 m in elevation prediction (error increases as function of elevation complexity). The 100 m × 100 m land use map was based on the *Arealstatistik 2004* data (source: Swiss Federal Statistical Office). Roughness lengths were computed based on this map following the classification suggested by Wieringa [1992, 1993] (supporting information Table S2 in the TR).

### 3.2. Grid Setting

A square domain of 25 km × 25 km surrounding Engelberg catchment was used (Figure 3). Two spatial and temporal resolutions were defined for the simulation: (i) a 2 km × 2 km and 5 min resolution was used for the precipitation and cloud cover variables, matching the weather radar spatiotemporal resolution and (ii) a 100 m × 100 m and 1 h resolution was used for all the other climate variables. The spatial resolution was chosen to be 100 m and not 25 m in order to further speed up simulation time and reduce data storage requirements.

### 3.3. Calibration

The calibration of the model components is described in detail in the Technical Reference and is not repeated here. In the following, only the modifications that were applied to the calibration procedure for the specific case study are discussed. Modification was applied only for the precipitation module due to the relatively short period of weather radar observations (8 years). Generally, in the calibration of the storm arrival process, the statistics for the wet and dry sequences are estimated using the weather radar. The main reason to prefer weather radar over rain gauges relies on the fact that a rain gauge represents only a point in the domain, thus it records only part of the precipitation over a given region, resulting in underestimation of both occurrence and length of the wet periods. However, in our case study, we could not use the weather radar to obtain the required dry-wet statistics because of the relatively short period of observation, which are insufficient to represent the natural variability of storm occurrence and duration. Thus, we have used the five rain gauges covering the domain to compile a time series of dry and wet conditions in the region of interest. Conditions are marked “wet” if at least one rain gauge was recording rainfall at a given time. Doing so, we compromised on the accuracy of the wet/dry sequence but increased our database (to 31 years), thus improving the representation of natural variability. Note that the simulation of rain fields has a temporal resolution of 5 min (corresponding to weather radar resolution), while the simulation of the storm arrival process is at the 10 min temporal resolution (corresponding to the rain gauge resolution).

The rainfall intensity estimated from the weather radar is binned in fixed intervals rather than being a continuous variable, this affects the calibration process biasing IMF and rainfall spatial CV estimations. However, in the current application these biases are relatively unimportant because the spatially homogeneous precipitation (in statistical terms) is subsequently filtered to account for observed spatial heterogeneity in precipitation occurrence and intensity as discussed below.

The filters describing the spatial variability in the probability of precipitation occurrence and precipitation intensity cannot be estimated for the Engelberg region directly from radar data (limited data availability) or rain gauges (too sparse). To overcome this issue, we assume that the probability of rainfall occurrence for

each grid cell in the domain is well described by the normalized daily rainfall precipitation occurrence computed from the gridded precipitation product (RhiresD) and use the latter to modify (filter) rainfall occurrence in the domain. The filter to account for spatial heterogeneity in the probability distribution of rainfall intensity for each grid cell was also computed based on a daily resolution rather than on a 5 min one. Specifically, a Generalized Pareto (GP) distribution is fitted to the daily rainfall data (above a threshold of  $1 \text{ mm d}^{-1}$ ) derived from the RhiresD product for each grid cell. During the simulation procedure, the nonhomogeneous spatial precipitation intensity filter is therefore applied on a daily basis. The rainfall is first simulated for a year period at 5 min temporal resolution, then aggregated to daily rainfall. Subsequently, a daily correction filter for the rainfall is obtained comparing the simulated daily distribution of precipitation with the GP distribution and this correction factor is applied back to the simulated 5 min rainfall depth.

#### 4. Validation

The performance of AWE-GEN-2d was tested for its ability to reproduce the observations for a number of climate variables (e.g., gridded precipitation, cloud cover, near-surface air temperature, and shortwave incoming radiation) at various temporal scales (i.e., from subdaily to annual) in the Engelberg region. In order to account for internal climate variability, 50 stochastic realizations, each 30 years long, were generated using AWE-GEN-2d to simulate meteorological variables over the domain. Common practice in studies of stochastic weather generators is to use the same data set for the calibration and validation processes [e.g., Entekhabi *et al.*, 1989; Ivanov *et al.*, 2007; Peleg and Morin, 2014; Racsco *et al.*, 1991], while validating for different statistics and time scales than the ones used for model calibration. An additional qualitative evaluation of model realism is shown in Movie S1 (supporting information) that illustrates the high-resolution simulations of some of the key climate variables generated by AWE-GEN-2d for the case study.

##### 4.1. Storm Arrival Process

AWE-GEN-2d was tested to reproduce the number and length of rainfall events on a monthly basis (Figure 4). For the majority of months, the mean and standard deviation of the simulations match very closely the observed data. One exception is represented by the month of June, in which the mean values are well preserved for both the occurrence (error of 3.1%) and length (error of 5.8%) of rainfall events, while the simulated standard deviation is larger than expected (by 60% and 32%, respectively).

##### 4.2. Mean Areal Statistics

A comparison between the radar/reanalysis observed and simulated distributions of *IMF*, *CAR*, and *WAR* on a monthly basis is shown in Figure 5, Figures S2 and S3, respectively (the prefix S stands for supporting information figure). AWE-GEN-2d performs generally very well in reproducing both the shape of the probability density function and the seasonality considering the relatively short period that was used for calibration (8 years).

The distribution of *IMF* is well simulated for the  $IMF < 5 \text{ mm h}^{-1}$  range (Figure 5), which represents most of the sample (up to the 0.995–0.997 quantile, depending on the month). However, the model underestimates the mean and standard deviation for all months. This indicates that the model is underestimating the extreme rainfall intensities (upper 0.003–0.005 percentiles) in the entire region. The comparison of the

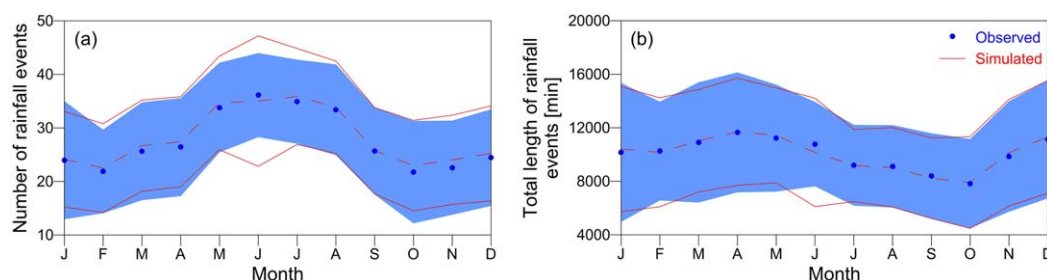


**Figure 4.** A comparison between observed and simulated (a) monthly number of rainfall events and (b) the total duration of rainfall. The blue dots and red dashed lines represent the observed and simulated mean values (respectively) and the bounded blue and red areas represent the observed standard deviation and the mean standard deviation of the simulated ensemble (respectively). Observed period covers 31 years of data (1983–2013) while simulations represent the mean of 50 realizations of 30 years each.

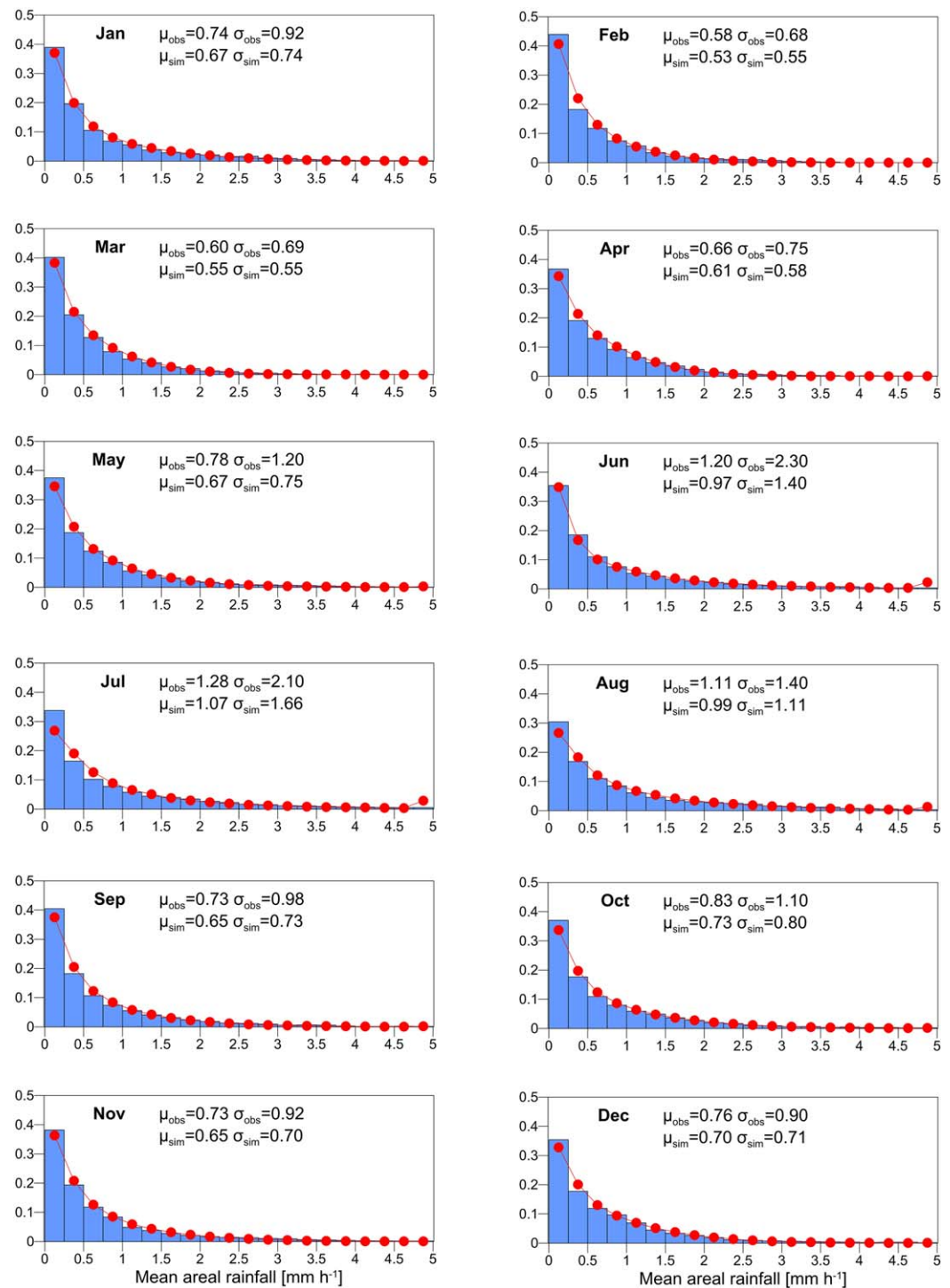


**Figure 5.** A comparison between observed (blue) and simulated (red) mean areal rainfall distribution for every month. The weather radar observed period covers 8 years of data (2003–2010), while simulations represent the mean of 50 realizations of 30 years each.

extreme rainfall intensity between the short observed period (8 years) and the much longer simulated period (30 years) is, however, forcefully limited.

The mean and standard deviation statistics are well preserved for CAR on a monthly basis (Figure S2). However, a consistent underestimation of overcast or nearly overcast conditions (cloud cover >0.9) and an overestimation of clear-sky occurrences (cloud cover <0.1) can be detected. These differences are typically small

and fall within the expected sampling error due to the short length of the data sample and the coarse resolution of the Merra product data (spatial extent of roughly  $50 \text{ km} \times 66 \text{ km}$ ).

The mean and standard deviation statistics are also well preserved for the *WAR* component (Figure S3). Minor differences exist between the observed and simulated distributions (mainly for the  $0.7 > \text{WAR} > 0.9$  range), and are within an acceptable error range (less than 3%).

We conclude that the areal rainfall statistics for the Engelberg region are well preserved by AWE-GEN-2d in most days, while to account for the extreme rainfall intensities at high-temporal resolution with a greater level of confidence a much longer radar observation data set would be likely necessary. Note that matching *IMF* radar rainfall at 5 min is not straightforward because the latter information is not used in the model calibration, while, the daily rainfall intensity statistics including extremes are reproduced almost exactly (see below), because of the application of the precipitation intensity filter to account for spatial heterogeneity at this resolution.

### 4.3. Gridded Precipitation

The median of the observed annual rainfall from the RhiresD product (32 years) was compared to the mean of the median annual rainfall that were simulated using AWE-GEN-2d (30 years  $\times$  50 realizations), allowing a cell-to-cell comparison (Figure 6). It is clear from the top part presented in Figure 6 that the filter is working well and the spatial pattern of the rainfall is preserved by AWE-GEN-2d, with the orographic effect well accounted for (see catchment topography in Figure 3). A grid cell comparison between the observed data and simulation (Figure 6, bottom) yields a very good match of the median annual rainfall for most grid cells (99% of the observed grid cells are within the simulated rainfall variability). The differences between the

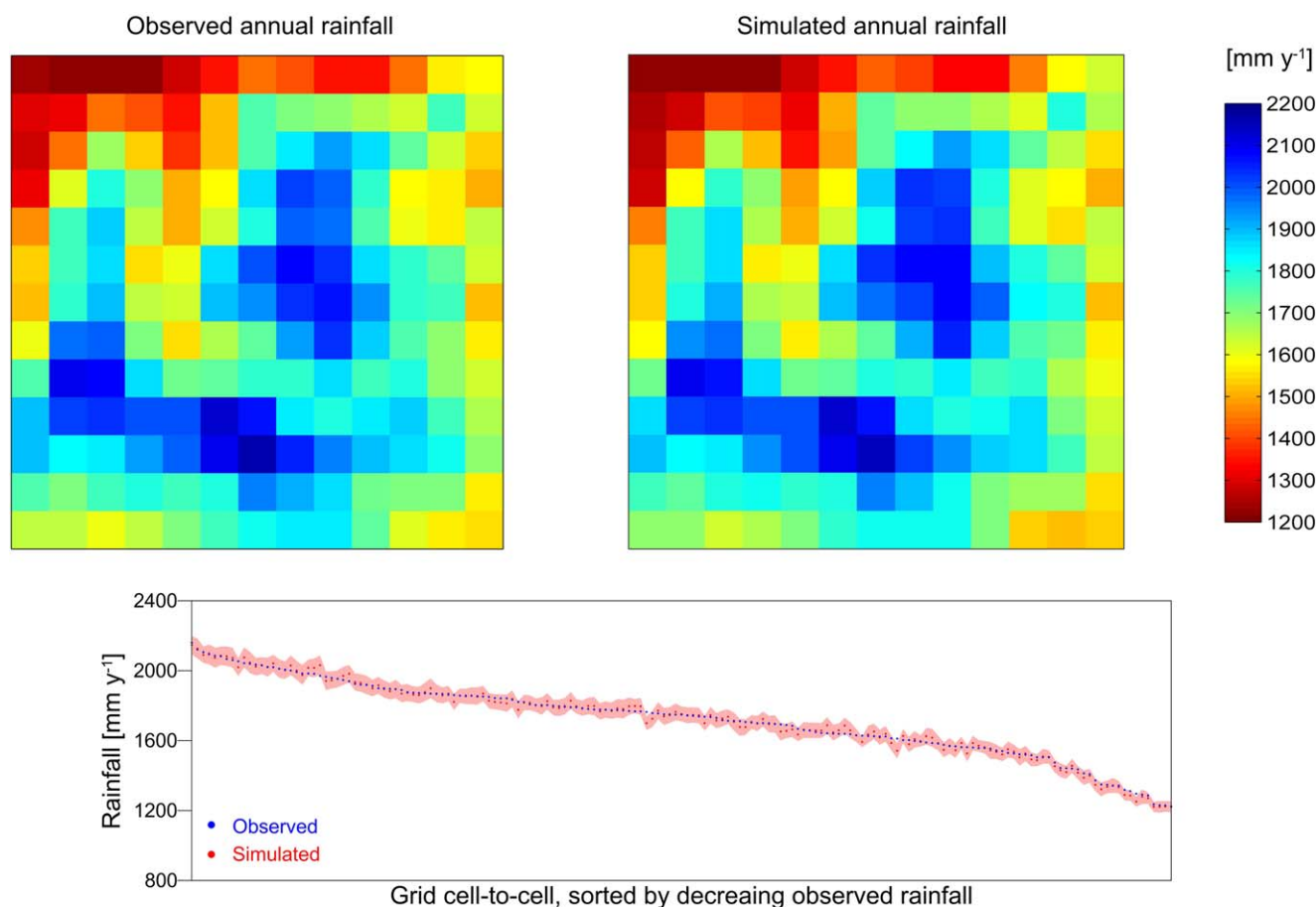


**Figure 6.** (top left) A comparison between the median observed annual rainfall, which covers 32 years of data (1981–2012), and (right) the mean of the median of the simulated annual rainfall generated using 50 realizations of 30 years each. The comparison between the observed (blue) and simulated (red) median annual rainfall for each grid cell within the domain is in the bottom. The shaded red range represents the standard deviation of the median for the 50 realizations.



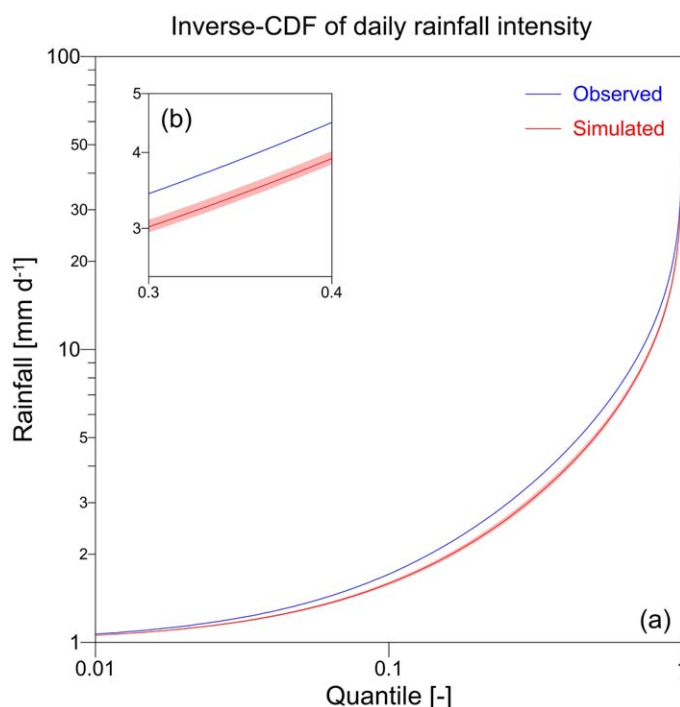


**Figure 7.** An inverse cumulative distribution function of the daily rain intensity over a randomly selected grid cell. The 0.01–1 quantile range is presented in Figure 7a and the 0.3–0.4 quantile range is zoomed in Figure 7b. The blue line represents 32 years of observed data (1981–2012) and the red line represents the median of 50 realizations of 30 years. The simulated 5–95 quantile range of the rainfall intensity of the 50 realizations is also presented (shaded red).

median observed and simulated annual rainfall are summarized in a histogram (Figure S4), showing errors that range between  $-4\%$  and  $3\%$ , with most of the errors distributed around the zero value. The reasons for this small error can be multiple, e.g., the detected underestimation of the length of rainfall events during the month of June and/or the underestimation of the daily rainfall intensity (Figure 7, see below). Note that the uncertainty of the median annual rainfall of a given grid cell in the observed 32 year period is in fact unknown, but is expected to be around  $10\%$  [Fatichi *et al.*, 2016]. It is reasonable to assume that the small error for the mean of the median annual rainfall obtained by AWE-GEN-2d ( $4\%$ ) is within this uncertainty range.

Rainfall intensity cannot be evaluated for this case study for the native 5 min temporal resolution (due to lack of data), however, it has been evaluated satisfactory at the subhourly time scale using

data from nearby locations in Switzerland [Paschalis *et al.*, 2013; Peleg *et al.*, 2017] and for generating extremes in a Mediterranean climate [see Peleg *et al.*, 2016]. The statistics for the rainfall intensity were evaluated at the daily scale by cumulating the simulated 5 min rainfall to daily resolution and conducting a cell by cell comparison with the RhiresD product. An example for this comparison is given in Figure 7 for a grid cell located in top left of the domain, used as illustrative example. The observed rainfall intensities are a bit higher than simulated rainfall intensities even when we account for stochastic variability. For example, for the 0.35 quantile (zoomed in Figure 7) the observed rainfall intensity is  $3.93 \text{ mm h}^{-1}$  while the simulated rainfall intensity is  $3.37\text{--}3.54 \text{ mm h}^{-1}$  (5–95 interval). This difference between the simulated and observed statistics is likely the result of using a GP distribution to fit the daily data. Alternative distributions such as the Mixed Exponential (ME) distribution [Wilks, 1999; Woolhiser and Roldn, 1982] for defining the correction filter can potentially improve daily precipitation fitting [Peleg *et al.*, 2015b].

#### 4.4. Advection

The observed and simulated wind direction and speed are plotted using a wind-rose diagram (Figure 8). A single simulated realization is used for validation. A small difference of  $0.8 \text{ m s}^{-1}$  is found between observed and simulated mean advection velocity, and a difference of  $5.6^\circ$  is found for the mean advection direction. The mean and standard deviation of the velocity and direction components are well reproduced, while a difference of  $17.5^\circ$  is found for the mode, skewing the peak of the simulated advection northward in comparison to the observed advection peak (Figure 8). The simulated distribution is much “smoother” in the direction component when compared to the observed distribution, as expected because of the difference between the short observed (8 years) and the long simulated (30 years) periods.

#### 4.5. Near-Surface Air Temperature

The median of the observed annual temperature from the TabsY product [Frei, 2014] was compared to the mean of the median annual temperature that was simulated using AWE-GEN-2d with a cell-to-cell comparison (Figure 9). The simulated grid was upscaled from 100 m resolution to 2 km resolution in order to match

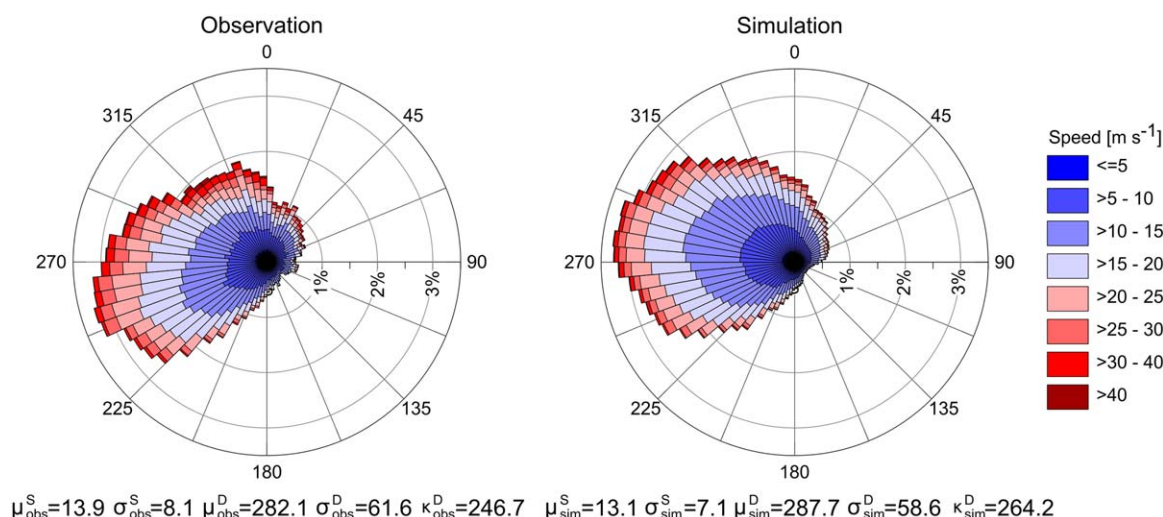


**Figure 8.** A comparison between (left) observed and (right) simulated wind direction and speed at the 500 hPa level. The observational period covers 8 years of data (2003–2010), while simulations represent one random realization of 30 years. The mean ( $\mu$ ), standard deviation ( $\sigma$ ), and mode ( $\kappa$ ) for the advection direction (D) and velocity (S) are mentioned.

the resolution of the observations. The spatial pattern and magnitude of the temperature is well reproduced by AWE-GEN-2d (top part presented in Figure 9). While comparing observations and simulations on a cell-to-cell basis (Figure 9, bottom) there are both an overestimation and underestimation of air temperature. The differences between observed and simulated values of the median annual temperature range from  $-2.6$  to  $+3^\circ\text{C}$  (Figure S5). Note that an accuracy of  $0.5$ – $1.5^\circ\text{C}$  is reported for the TabsY product [Frei,

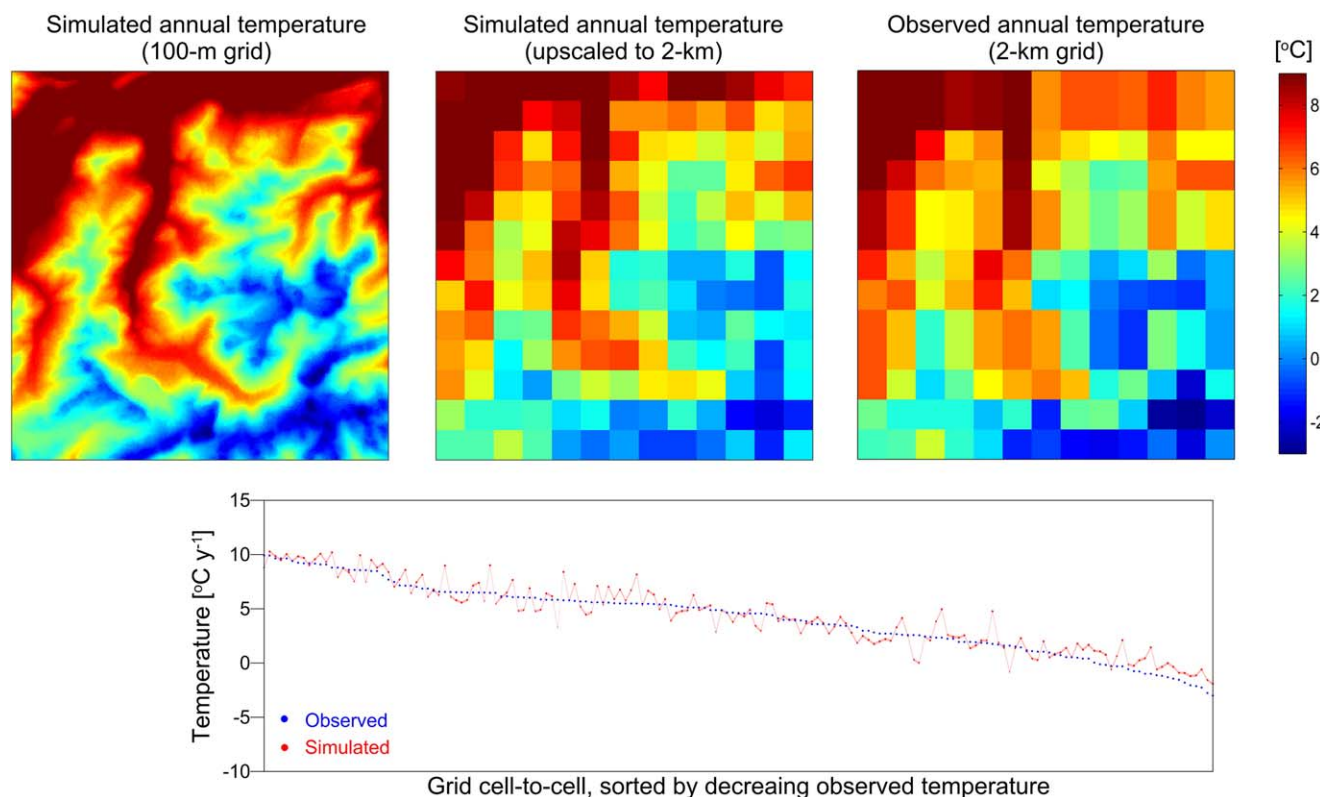


**Figure 9.** (top right) A comparison between the median observed annual temperature, which covers 32 years of data (1981–2012), and (left) the mean of the median simulated annual temperature generated using 50 realizations of 30 years each. The simulated grid was upscaled from (top left) 100 m resolution to (middle) 2 km resolution to match the resolution of observations. A comparison between the observed (blue) and simulated (red) median annual temperature for the grid cells in the domain is in the bottom. The shaded red range represents the standard deviation of the median for the 50 realizations.

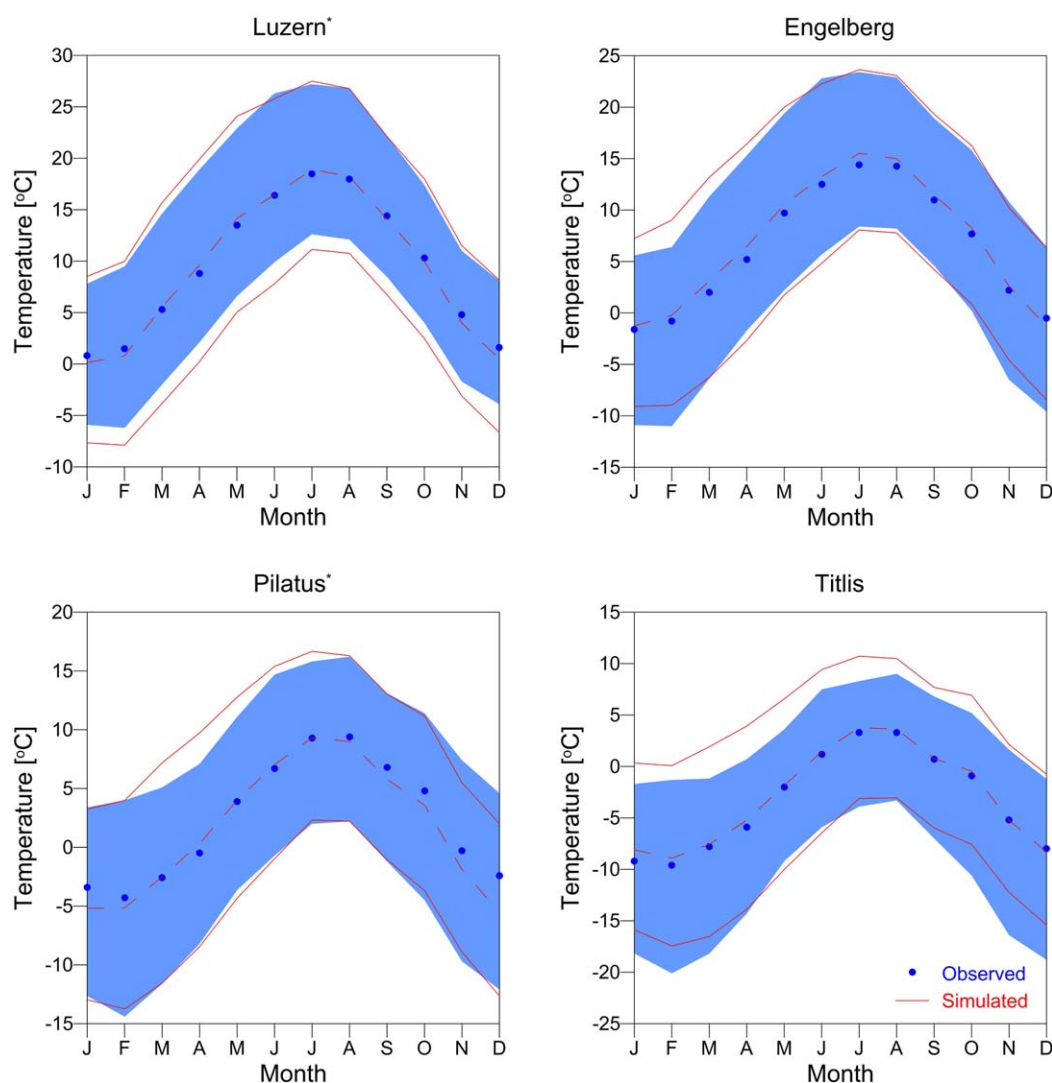


**Figure 10.** A comparison between observed and simulated near-surface (2 m) air temperature for each month. The blue dots and red dashed lines represent the observed and simulated median values (respectively) and the bounded blue and red areas represent the observed and simulated 5–95 quantile range (respectively). The observed period covers 32 years of data (1981–2012), while simulations represent the mean of 50 realizations of 30 years each.

2014] and 89% of the grid cells falls in the  $\pm 1.5^{\circ}\text{C}$  error range (Figure S5). In total, the average difference between observed and simulated median annual temperature over the domain is  $0.2^{\circ}\text{C}$ , which can be considered highly satisfactory.

The seasonal variation of median temperature and its 5–95 quantile range, comparing observed (point scale) and simulated (100 m grid cell) data is presented in Figure 10. Engelberg and Titlis stations are located within the domain area, while Luzern and Pilatus stations (marked with asterisks in the figures) are a few kilometers outside the domain. In order to compare the latter stations, the grid cells with the closest elevation to Luzern and Pilatus were selected. AWE-GEN-2d reproduces well the monthly statistics for the stations, the maximum temperature error is  $3.1^{\circ}\text{C}$  in the month of December for Pilatus, while most differences are smaller than  $0.5^{\circ}\text{C}$ . Some discrepancy in the median and quantile range is expected considering the scale difference between the grid cell and the station.

A comparison of the daily maximum (Figure S6) and daily minimum (Figure S7) temperatures between the observed data and simulation was also carried out. The daily maximum temperature statistics are well reproduced for Luzern and Engelberg stations in the different months. There is a slight overestimation of the daily maximum temperature for the two mountain stations, Pilatus (maximum overestimation of  $2.85^{\circ}\text{C}$

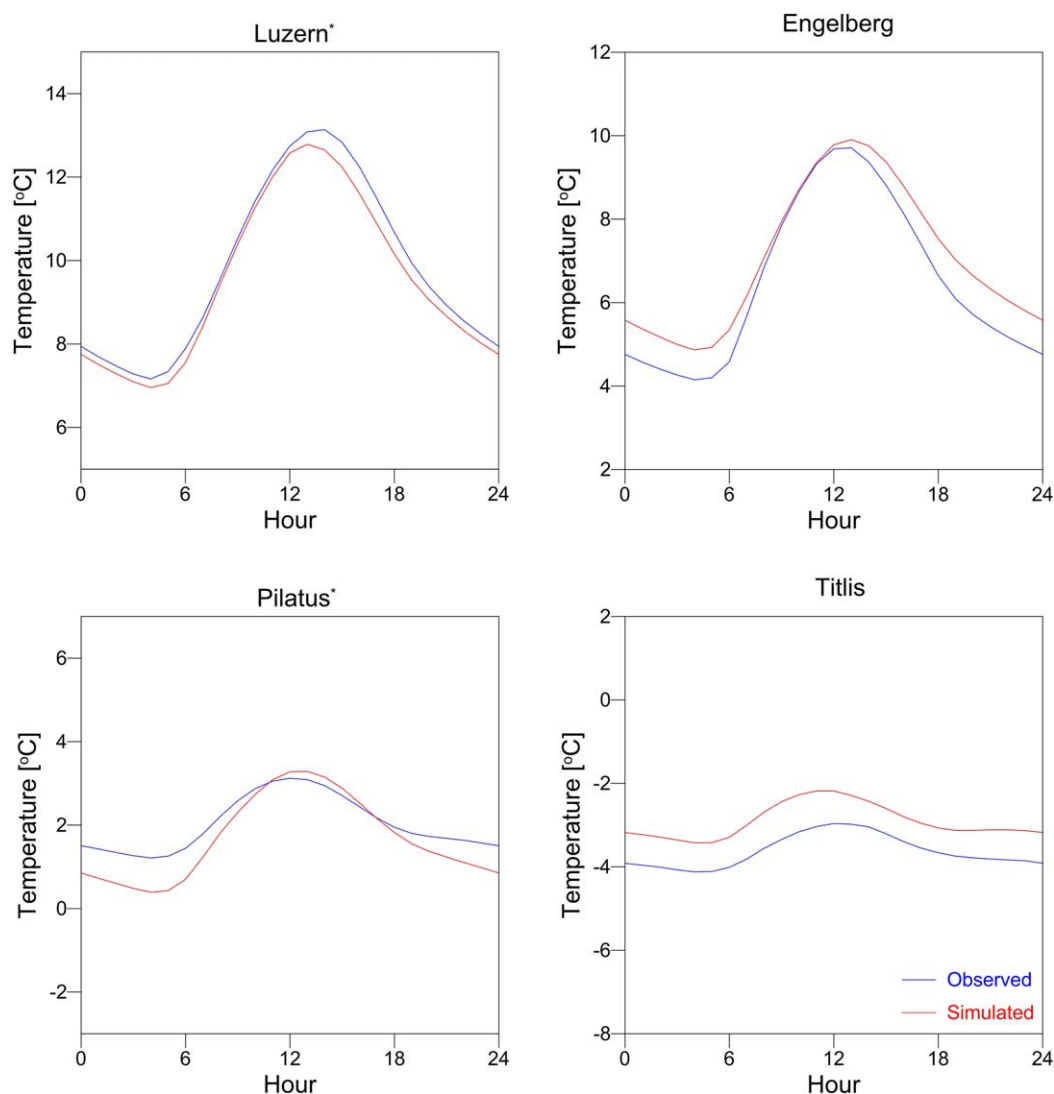


**Figure 11.** A comparison between observed (blue) and simulated (red) average daily cycle of near-surface (2 m) air temperature. The observed period covers 32 years of data (1981–2012), while simulations represent the mean of 50 realizations of 30 years each.

in April) and Titlis (maximum overestimation of 2.58°C in March). Engelberg is well simulated in terms of daily minimum temperature, as well as is Titlis, with only a minor underestimation during summer months. On the other hand, the model underestimates the daily minimum temperatures for Luzern and Pilatus (maximum underestimation of 1.97 and 2.84°C, respectively, in December). However, in general AWE-GEN-2d reproduces the daily maximum and minimum temperatures reasonably well, considering the above mentioned scale differences.

The average daily cycle of temperature is also examined (Figure 11). For Luzern, the simulated average daily cycle of temperature fits the observed data very well, with a maximum difference of  $-0.64^{\circ}\text{C}$ . For Engelberg and Pilatus, the daily cycle is captured during daytime, while during night an overestimation (underestimation) with a maximum difference of  $0.93^{\circ}\text{C}$  ( $-0.82^{\circ}\text{C}$ ) for Engelberg (Pilatus) is detected. The temperature average daily cycle for Titlis is overestimated throughout the day, with a maximum difference of  $0.9^{\circ}\text{C}$  detected at 10–11 A.M. For all stations, differences in the temperature cycle between observed data and simulation are always smaller than  $1^{\circ}\text{C}$ .

The fitting of the entire probability density function of temperature for the four stations is shown in Figure S8. The shape of the temperature distribution is satisfactorily reproduced, as well as the main statistics.



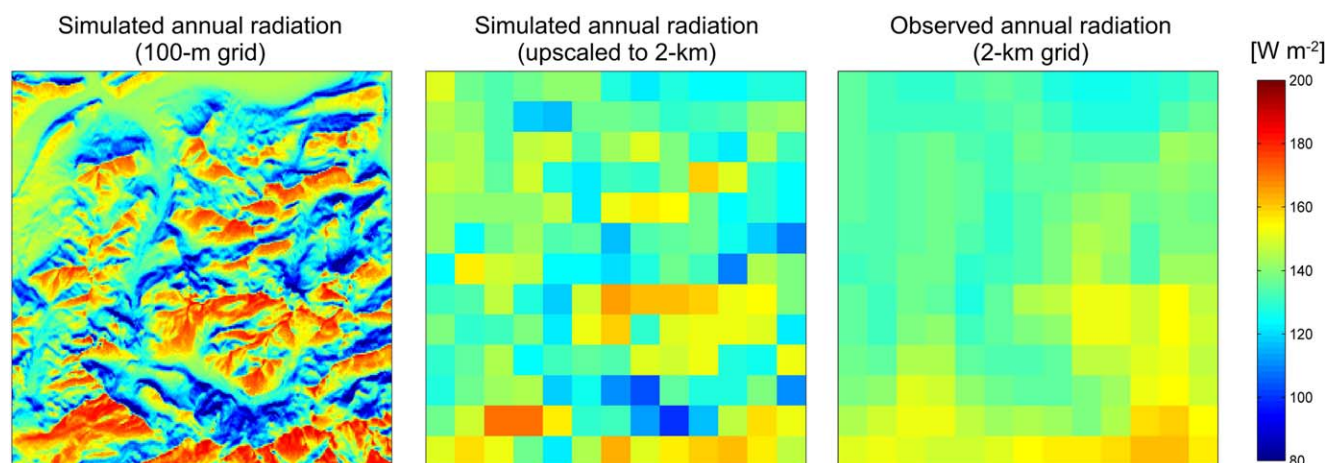


**Figure 12.** (right) A comparison between the mean observed annual incoming shortwave radiation, which covers 9 years (2004–2012), and (left) the mean of the simulated annual incoming shortwave radiation generated using 50 realizations of 30 years each. (middle) The simulated grid was upscaled from 100 m resolution to 2 km resolution to match the resolution of the SIS product.

#### 4.6. Shortwave Radiation

The mean of the observed annual radiation (9 years) from the SIS product [Stöckli, 2013] was compared to the mean (50 realizations  $\times$  30 years) of annual radiation that was simulated using AWE-GEN-2d (Figure 12). Simulations were upscaled from 100 m resolution to 2 km resolution in order to match the resolution of the observed data. The pattern of the radiation simulated by AWE-GEN-2d introduces a spatial variability that is not captured by the SIS product (but is expected in reality), with high radiation over the mountain tops and south-slopes (maximum annual average of  $191 \text{ W m}^{-2}$ ) and lower radiation along the valleys and north-slopes (minimum annual average of  $54 \text{ W m}^{-2}$ , Figure 12). The spatial variability of the simulated radiation is considerably larger than in the SIS product. This is likely due to the coarse resolution of SIS, which limits its ability to resolve detailed features, as mountain peaks and steep valleys, in a complex terrain (e.g., mean

monthly bias comparing SIS grid cell over Pilatus station is  $13 \text{ W m}^{-2}$ ) [see Stöckli, 2013]. A cell-to-cell comparison between the simulated and observed grid cells should therefore be treated very carefully. Comparing observed and simulated mean annual radiation over the entire domain produces a difference of  $2.06 \text{ W m}^{-2}$  (1.5% error), which is within the limit of the observational error.

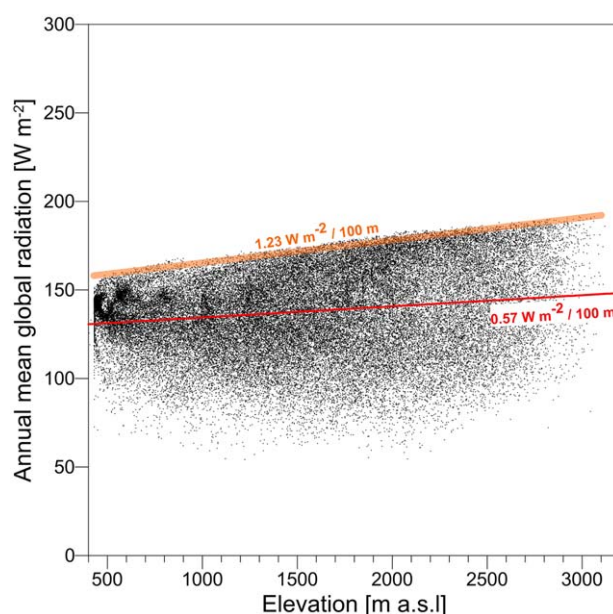


**Figure 13.** Simulated annual mean incoming shortwave radiation as a function of elevation in the domain, obtained from each grid cell. The red line represents the mean radiation gradient with elevation over the entire domain and the orange line represents the radiation gradient only for the upper envelope (2%) of points.

The gradient of annual mean simulated incoming shortwave radiation with elevation is presented in Figure 13. The mean gradient of radiation over the domain is  $0.57 \text{ W m}^{-2}/100 \text{ m}$ , considering the entire domain with valleys, slopes, and mountain tops. Considering the gradient of radiation only for the upper envelope in the domain, a gradient of  $1.23 \text{ W m}^{-2}/100 \text{ m}$  is obtained. This gradient represents the grid cells that are mostly exposed to incoming shortwave radiation, i.e., grid cells that represent either mountain tops or southern slopes that are not shaded by the surrounding terrain. This

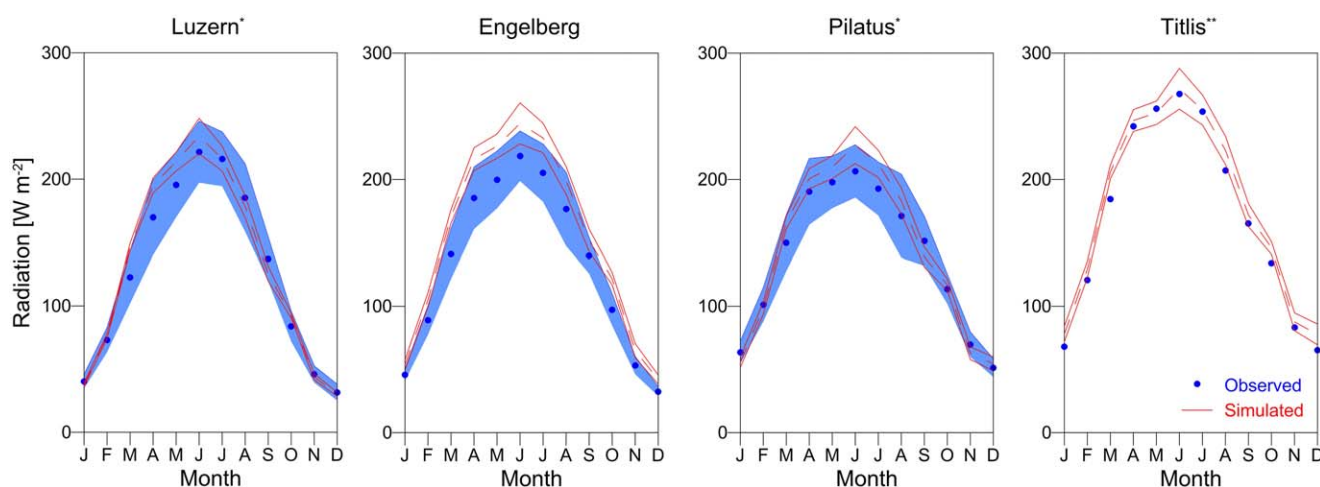


**Figure 14.** A comparison between observed and simulated incoming shortwave radiation for each month. The blue dots and red dashed lines represent the observed and simulated mean values (respectively) and the bounded blue areas and red lines represent the observed and simulated standard deviation of the monthly values (respectively). The observed period covers 15 years of data (2000–2014), except for Titlis station (3 years only are available). Simulations represent the mean of 50 realizations of 30 years each.

gradient is very close to the  $1.3 \text{ W m}^{-2}/100 \text{ m}$  gradient observed by *Marty et al.* [2002] using several stations in the Alpine region. Considering the upper envelope only for grid cells with slope lower than 2%, which is equivalent to selecting only the flat mountain tops, provides a simulated gradient of  $1.43 \text{ W m}^{-2}/100 \text{ m}$ .

The observed and simulated seasonal variability in radiation is also presented (Figure 14). Luzern and Pilatus stations are not part of the domain area, therefore, the closest grid cells with an equivalent elevation and as similar as possible terrain characteristics (expressed by similarity in sky view factor and aspect) were chosen. Titlis station has a radiation record for only 3 years as the measuring device was recently installed, therefore, no standard deviation is presented for the observations. Generally, the seasonal cycle is reproduced well by AWE-GEN-2d, considering the scale difference between the grid cells and the point location. However, the variability of the monthly radiation (expressed by the standard deviation) reproduced by the WG is considerably lower than the observed one, especially for the period between September and March when the sun height is relatively low. A better representation of the radiation, in terms of both accuracy and variability, can be obtained with AWE-GEN-2d by using a finer spatial resolution to account for the terrain effects more precisely and by considering the currently constant atmospheric components (e.g.,  $\text{O}_3$  and  $\text{NO}_2$ ) variant in time, accounting for their seasonality.

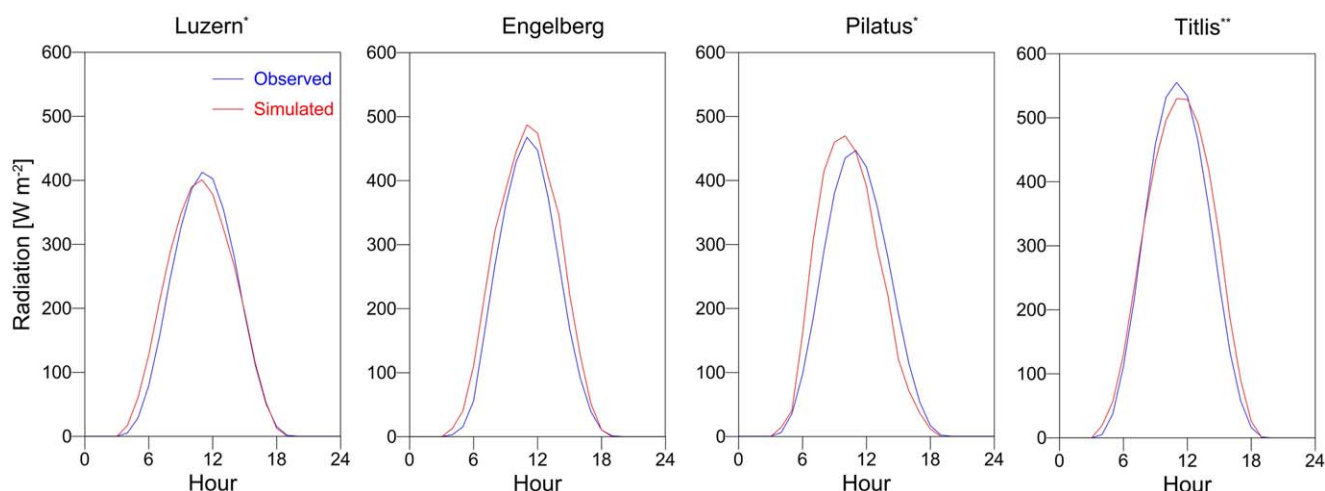


**Figure 15.** A comparison between observed (blue) and simulated (red) average daily cycle of incoming shortwave radiation. The observed period covers 15 years of data (2000–2014) for Luzern, Engelberg, and Pilatus and 3 years of data (2013–2015) for Titlis. Simulations represent the mean of 50 realizations of 30 years each.

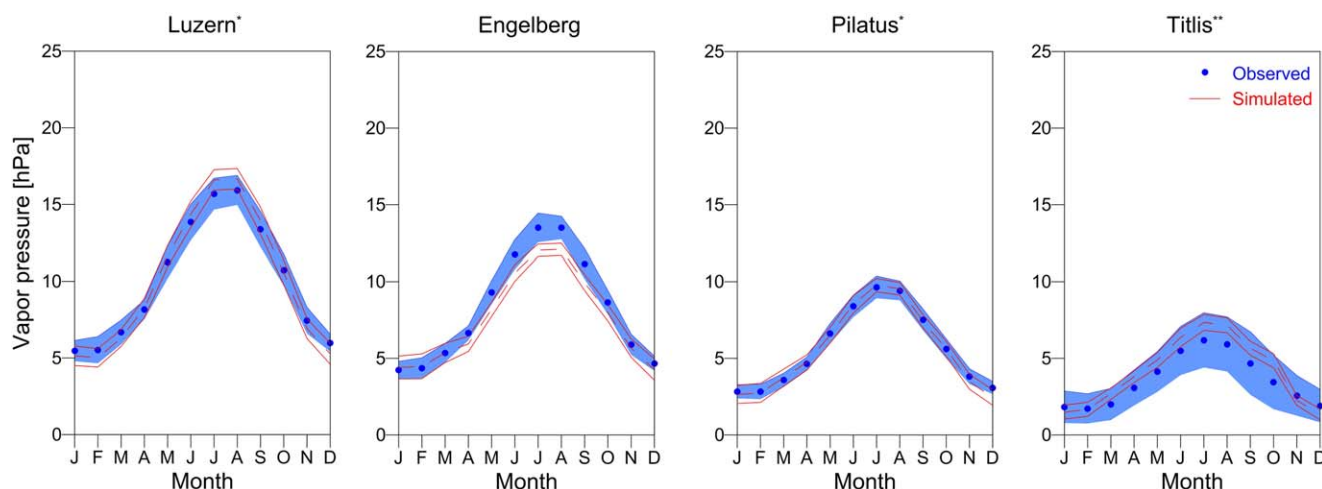


**Figure 16.** A comparison between observed and simulated vapor pressure for each month. The blue dots and red dashed lines represent the observed and simulated mean values (respectively) and the bounded blue areas and red lines represent the observed and simulated standard deviation of the monthly values (respectively). The observed period covers 30 years of data (1985–2014) for Luzern, Engelberg, and Pilatus and 10 years of data (2005–2015) for Titlis. Simulations represent the mean of 50 realizations of 30 years each.

The radiation average daily cycle is shown in Figure 15. For Luzern and Engelberg, the simulated average daily cycle of radiation fits the observed data well. The largest differences in radiation (maximum difference are 55.3 and 74.3  $\text{W m}^{-2}$  for Luzern and Engelberg, respectively) result from the spatial scale mismatch between grid and station and from a small time lag between observed data and simulation. The simulated daily cycle for Pilatus station slightly precedes the observed cycle, resulting in a maximum difference of 124.7  $\text{W m}^{-2}$ . The chosen grid cell that represents Pilatus does not share exactly the topographic characteristics (e.g., slope aspect) of the station position and this can explain the above mentioned difference. Titlis station is also presented in Figure 15, showing a good fit between observed data and simulation (a maximum difference of 73.8  $\text{W m}^{-2}$ ), but for a short observational record of 3 years.

#### 4.7. Vapor Pressure and Relative Humidity

The observed and simulated seasonal variation of vapor pressure is presented in Figure 16. The seasonal variation of vapor pressure is well reproduced for Luzern and Pilatus. For Engelberg, an underestimation is detected for the period between May and September while for Titlis an overestimation is detected for the period between March and October. A comparison between observed and simulated vapor pressure distribution is given in Figure 17. For Luzern and Pilatus, the shape of the vapor pressure distribution and the

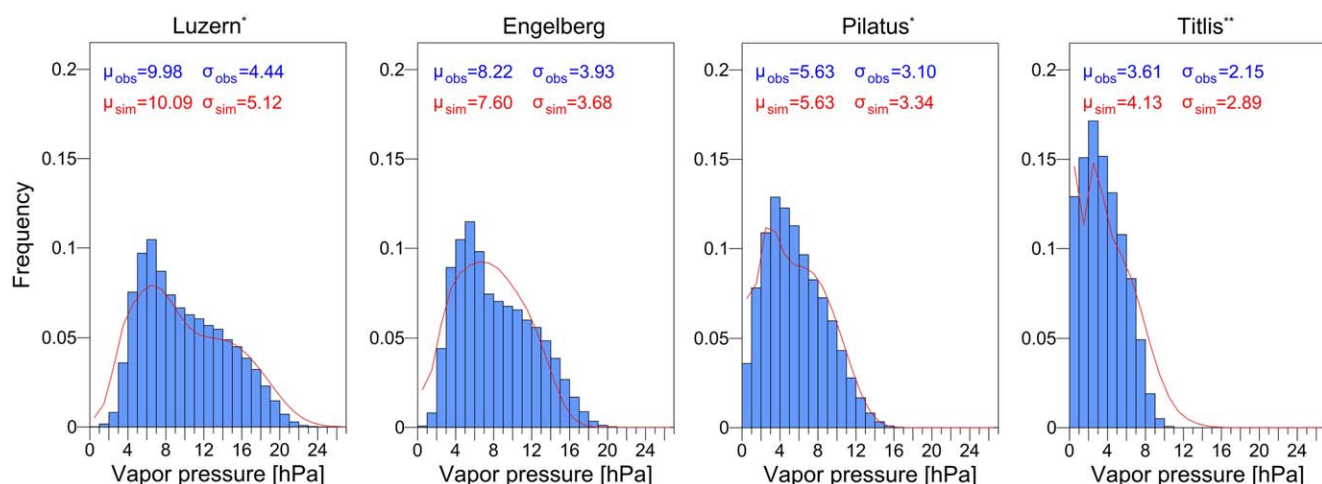


**Figure 17.** A comparison between observed (blue) and simulated (red) vapor pressure distribution. The observed period covers 30 years of data (1985–2014) for Luzern, Engelberg, and Pilatus and 10 years of data (2005–2015) for Titlis. Simulations represent the mean of 50 realizations of 30 years each.

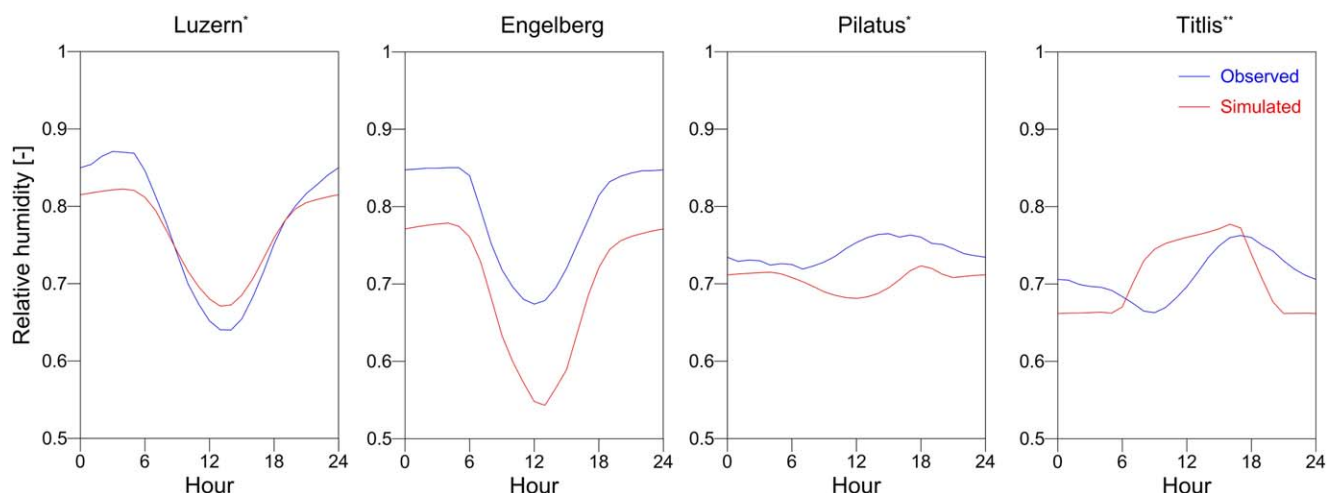


**Figure 18.** A comparison between observed (blue) and simulated (red) average daily cycle of relative humidity. The observed period covers 30 years of data (1985–2014) for Luzern, Engelberg, and Pilatus and 10 years of data (2005–2015) for Titlis. Simulations represent the mean of 50 realizations of 30 years each.

principal statistics are satisfactorily reproduced, while for Engelberg and Titlis, the shape of the distribution is mostly captured, but the mean vapor pressure is underestimated (Engelberg) by 0.62 hPa and overestimated (Titlis) by 0.52 hPa.

A comparison between observed and simulated average daily cycle of relative humidity is presented in Figure 18. For Pilatus and Luzern the daily cycle is well represented, while for Engelberg the daily cycle is underestimated (by up to 13% difference). The daily cycle for Titlis is not well captured, as the simulated rising limb starts 3 h earlier than the observed rising limb and the simulated recession limb is much steeper than the observed one. A comparison between observed and simulated relative humidity probability distributions is presented in Figure S9. AWE-GEN-2d reproduces the shape of the distribution and the principal statistics satisfactorily for Luzern, Pilatus, and Titlis with small overestimations of low relative humidity values, while for Engelberg the probability distribution is biased toward lower values.

#### 4.8. Atmospheric Pressure

The atmospheric pressure distributions for Luzern, Engelberg, and Pilatus are presented in Figure 19. For all stations, AWE-GEN-2d satisfactorily reproduces the shape of the distribution; the mean atmospheric pressure is well preserved while the standard deviation is underestimated by ~10%.

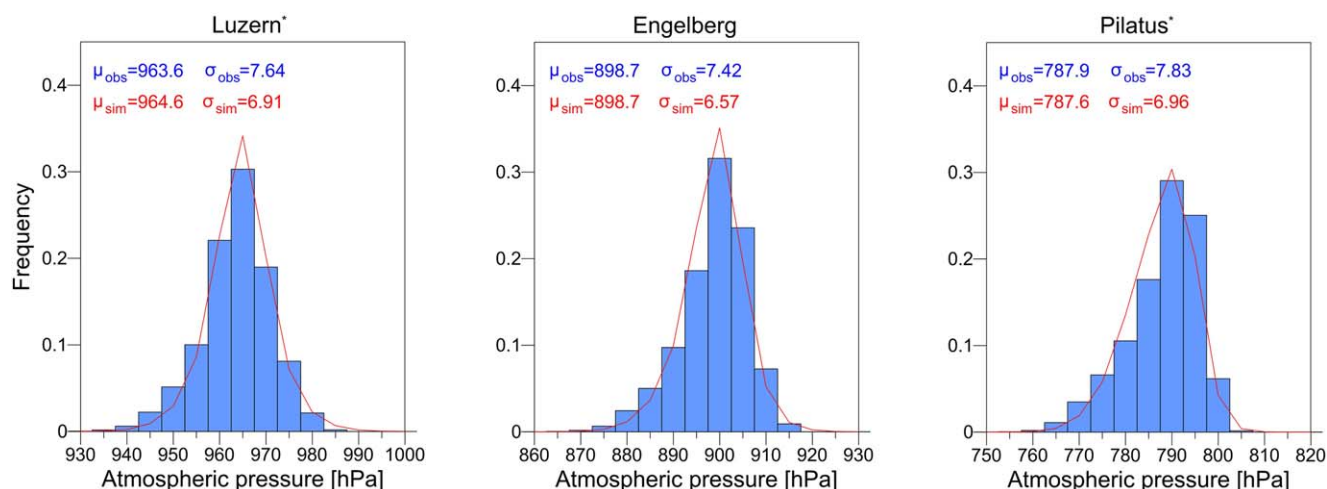


**Figure 19.** A comparison between observed (blue) and simulated (red) atmospheric pressure distribution. The observed period covers 11 years of data (2004–2014), while simulations represent the mean of 50 realizations of 30 years each.



#### 4.9. Near-Surface Wind Speed

The complex terrain of the case study produces low wind velocities along the valleys (e.g., Engelberg station) but strong winds are observed in the mountaintop stations (e.g., Titlis). The validation for the near-surface wind speed (at 2 m) was done by comparing observed data from ground stations to their corresponding simulated values in the specific grid cells. Two types of simulations were compared, (i) a case where terrain effects beyond elevation are not considered (Figure S10) and (ii) a case where terrain effects (slope, aspect) are explicitly included to modify the near-surface wind speed field (Figure 20). Near-surface wind speed at Luzern and Engelberg is well represented in both cases (an annual bias of  $-0.05$  and  $-0.02$   $\text{m s}^{-1}$  for the first case, and an annual bias of  $-0.18$  and  $-0.29$   $\text{m s}^{-1}$  for the second case, respectively), while for Pilatus and Titlis (both located at mountain tops) wind speed is underestimated for the case without terrain effects (an annual bias of  $-0.46$  and  $-0.88$   $\text{m s}^{-1}$ , respectively) and overestimated for the case with terrain effects (an annual bias of  $0.68$  and  $0.64$   $\text{m s}^{-1}$ , respectively).

Hourly extreme wind speeds are strongly affected by wind gusts. Wind gusts are characterized with an intense (larger than  $10$   $\text{m s}^{-1}$ ), but short (lasting from a second to several minutes), bursts of winds. As the temporal resolution of AWE-GEN-2d is hourly, wind gusts cannot be simulated by the model, and thus

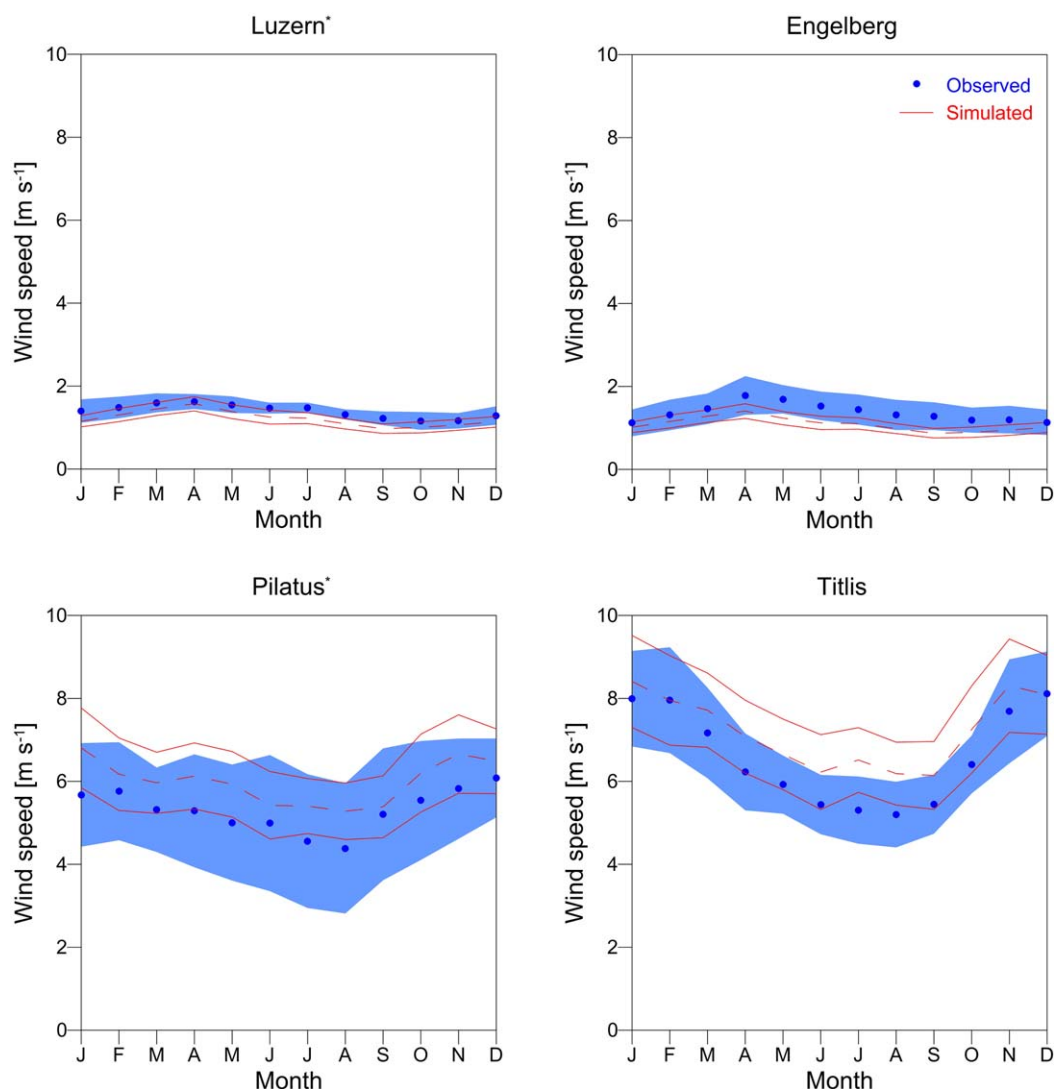


**Figure 20.** A comparison between observed and simulated near-surface wind speed (at 2 m), considering terrain effects, for each month. The blue dots and red dashed lines represent the observed and simulated mean values (respectively) and the bounded blue areas and red lines represent the observed and simulated standard deviation of the monthly values (respectively). The observed period covers 16 years of data (1999–2015), while simulations represent the mean of 50 realizations of 30 years each.

**Table 5.** A Comparison Between the Observed and Simulated Means of Daily Temperature Amplitude,  $\Delta T_{day}$ , Daily Shortwave Radiation,  $RSW_{day}$ , and Daily Relative Humidity,  $RH_{day}$ , During Rainy (Precipitation  $> 0$  mm) and Dry Days for the Engelberg Station

Variable	Rainy Days		Dry Days	
	Observed	Simulated	Observed	Simulated
$\Delta T_{day}$ ( $^{\circ}\text{C}$ )	7.7	8.0	10.4	8.9
$RSW_{day}$ ( $\text{W m}^{-2}$ )	104	138	156	175
$RH_{day}$	0.84	0.70	0.72	0.69

few locations. For a better representation of the wind speed over slopes and ridge tops, a finer spatial resolution would be probably necessary along with a fine-tuned calibration of the slope and curvature weights in the terrain correction factors.

#### 4.10. Covariance Between Variables

An explicit analysis of cross correlation between some of the climate variables is provided in the following. Table 5 shows a comparison between the observed and simulated means of daily temperature amplitude,  $\Delta T_{day}$ , daily shortwave radiation,  $RSW_{day}$ , and daily relative humidity,  $RH_{day}$ , during rainy (precipitation  $> 0$  mm) and dry days for Engelberg station. AWE-GEN-2d tends to underestimate the differences between rainy and dry days. The observed daily temperature amplitude is increased by  $2.7^{\circ}\text{C}$  comparing rainy days to dry days, while the simulated daily temperature amplitude is increased only by  $0.9^{\circ}\text{C}$ , the observed daily shortwave radiation increases by  $52 \text{ W m}^{-2}$  comparing to a simulated increase of  $37 \text{ W m}^{-2}$ , and the observed relative humidity significantly decreases comparing rainy and dry days while the simulated relative humidity remains similar. These shortcomings are a consequence of the structure of AWE-GEN-2d that only implicitly accounts for the influence of precipitation on the other variables (via cloudiness). This linkage is also explicitly accounted for at the hourly and not at the daily scale. Therefore, more complex cross correlations occurring in a longer temporal range remain challenging to reproduce. For instance, Table 6 shows an overview of cross correlations at the daily scale between some of the variables. The main cross correlations are captured at lag-0. Note that AWE-GEN-2d is not explicitly designed to reproduce these cross correlations at the daily time scale. Although differences can be noticed (particularly for the air temperature daily amplitude—daily relative humidity cross correlation), the results, which emerges solely from the weather generator structure, can be considered quite satisfactory.

### 5. AWE-GEN-2d Advantages and Limitations

The major climatic variables required by spatially explicit numerical models of environmental systems, with hydrological, ecological, geomorphological, and agricultural studies in mind, are precipitation, near-surface air temperature, and incoming shortwave radiation [e.g., *Fatichi et al.*, 2015; *Schlabing et al.*, 2014; *Semenov*, 2006; *Wheater et al.*, 2005]. As shown in the model test, it is apparent that precipitation and near-surface air temperature variables are generated by AWE-GEN-2d with a high level of accuracy, sufficient for most practical applications. AWE-GEN-2d is able to reproduce well the spatial and temporal variability and the

extreme wind speeds are very badly reproduced. For example, the hourly extreme wind speed observed at Engelberg station is  $16 \text{ m s}^{-1}$  when gusts are considered and  $6.3 \text{ m s}^{-1}$  when gusts are excluded from the observation (gusts are affecting 3% of the hourly data). The simulated hourly extreme wind speed is 6 and  $5.1 \text{ m s}^{-1}$  in the two analyzed cases.

Generally, AWE-GEN-2d represents the near-surface wind speed reasonably well even though a detailed validation is challenging with the data available at

**Table 6.** A Comparison Between the Observed and Simulated Cross Correlation of Daily Temperature Amplitude and Daily Cloudiness,  $\Delta T_{day} - CAR_{day}$ , Daily Shortwave Radiation and Daily Cloudiness,  $RSW_{day} - CAR_{day}$ , Daily Shortwave Radiation and Daily Wind Speed,  $RSW_{day} - WS_{day}$ , Daily Temperature Amplitude and Daily Relative Humidity,  $\Delta T_{day} - RH_{day}$ , and Daily Temperature Amplitude and Daily Rainfall,  $\Delta T_{day} - P_{day}$ , for the Engelberg Station

Variable	Lag-0		Lag-1		Lag-2	
	Observed	Simulated	Observed	Simulated	Observed	Simulated
$\Delta T_{day} - CAR_{day}$	-0.57	-0.26	-0.19	-0.04	-0.04	-0.02
$RSW_{day} - CAR_{day}$	-0.41	-0.41	-0.15	-0.08	-0.02	-0.05
$RSW_{day} - WS_{day}$	0.2	0.1	0.2	0.14	0.17	0.14
$\Delta T_{day} - RH_{day}$	-0.63	-0.16	-0.39	-0.11	-0.19	-0.07
$\Delta T_{day} - P_{day}$	-0.24	-0.14	0.01	-0.04	0.06	-0.01

principal statistics for these variables. The incoming shortwave radiation is also well reproduced, but it is challenging to perform a detailed spatial comparison with current available observations due to the coarse resolution of existing distributed data set such as SIS (Figure 12).

The other simulated variables (i.e., vapor pressure, relative humidity, atmospheric pressure, and near-surface wind speed) were compared to point locations, either using the corresponding grid cell in the domain or using a grid cell with similar characteristics (elevation, sky view factor, and aspect) for stations located outside the domain. Generally, AWE-GEN-2d reproduces quite well a large number of statistics for the above mentioned climate variables but cannot reproduce all statistics simultaneously equally well for the four local stations. The level of satisfaction is, in fact, variable with the location and is influenced by specific local terrain features. Likely, a better representation of the climate for such a complex terrain can be achieved by using an even finer spatial resolution, with the trade-off of a considerably longer computation time.

Advection is applied homogeneously to all grid cells in the domain. This means that the entire field moves in the same direction and with the same velocity [as in *Paschalis et al.*, 2013; *Pegram and Clothier*, 2001b; *Peleg and Morin*, 2014] and no local rotations or deviations are allowed. The assumption that the advection is homogenous is not valid over large domains, e.g., tens of kilometers, but is used in AWE-GEN-2d as a compromise between computational time and realism and for the sake of preserving the spatial structure of the precipitation fields.

Different synoptic systems and precipitation types (e.g., stratiform versus convective) are not explicitly simulated in this version of AWE-GEN-2d but are implicitly simulated due to the seasonality in the input variables (e.g., statistics of convective precipitation will not be simulated during winter). A component can be added to the storm arrival process (section 2.1.1) to differentiate the wet/dry periods by synoptic types and to determine the type of precipitation to be simulated [as in *Peleg and Morin*, 2014; *Peleg et al.*, 2015a] and will be considered in future developments of the model. Adding this component will allow a better representation of the precipitation, cloud cover, and advection variables (that can be classified in weather types using observations) and will influence the other climate variables through the simulation chain.

The variability that occurs repeating single realizations of 30 years (i.e., the ensemble of 50 members) allows to capture the internal climate variability for such a period. However, WGs typically suffer of the overdispersion problem, they often underestimate natural variability at intermediate time scales (e.g., monthly or annual) [Katz and Parlange, 1998]. Encouraging examples using AWE-GEN were shown to solve overdispersion issues and reproducing the interannual variability well [e.g., *Fatichi et al.*, 2011; *Fatichi and Ivanov*, 2014] and similar solutions can be applied in AWE-GEN-2d. Additionally, WGs can reproduce the variability that is related to the chaotic nature of climate, i.e., stochastic in nature. However, they cannot reproduce multidecadal variability when it is associated to deterministic nonstationary processes such as changes in ocean circulation, volcanic activity, changes in carbon dioxide concentration, or solar cycle variability. Non-stationarity can only be captured by reparameterizing the model.

The climate variables generated by AWE-GEN-2d are saved as 3-D array (two spatial dimensions and a time dimension). As in other climate models [Prein et al., 2015], saving data demands enormous resources in terms of available storage space and is often a bottleneck that slows WG performance. Post processing is therefore suggested, for some of the climate variables, as an integrated part of AWE-GEN-2d, allowing the user to save only the required variables. Moreover, it is suggested that an expert user will need to tailor AWE-GEN-2d output to the specific input format required by his/her impact model. An example of some of the key climate variables generated by AWE-GEN-2d is given in a short video entitled *AWE-GEN-2d Introduction*, which is included in the supporting information. Additionally, Figure 2 illustrates the joint generation of the climate variables by AWE-GEN-2d for a given grid cell in the domain (upper left grid cell) and for a random week in July.

For the presented case study AWE-GEN-2d was run on an Intel Xeon 3.1 GHz machine with 20 threads and 128 GB of memory. One hundred sixty-nine grid cells were included for the simulation of the precipitation grid and 62,500 grid cells were included for the simulation of the other climate variables (e.g., near-surface temperature and radiation). One year of simulation is composed of 105,120 five minute time steps (for precipitation) and 8760 hourly time steps (for all other climate variables). The average running time of AWE-GEN-2d to simulate 1 year of meteorological variables, including saving all data, is close to 8 min. This is substantially faster than the computational time needed by any climate or meteorological model that is

producing gridded data [Prein *et al.*, 2015]. Such a speed allows generating many realizations of a given climate in order to account for the natural (stochastic) climate variability required by impact studies. The capability to easily deal with stochastic variability but still concurrently and reasonably reproduce 2-D fields of several meteorological variables is considered the major strength of AWE-GEN-2d when compared with alternative approaches and ultimately the reason why we need WGs.

There is a limitation in the domain extent that AWE-GEN-2d can simulate. This is for two reasons. The statistics derived from observed data must be representative of the entire domain and for large domains this is not the case. For example, the temperature lapse rate can differ substantially for nearby catchments in areas with complex terrain [Frei, 2014], or storm advection cannot be considered uniform across the domain. The second reason is the availability of computer resources. The size of the domain is limited by the memory available on a given machine. For a machine with a 128 GB of memory, for example, a spatial extent of  $400 \times 400$  grid cells will be close to the upper limit (when coding with Matlab). The size of the domain will be then dependent on the spatial resolution selected by the user. If grid cell resolution is set to 100 m than a  $40 \text{ km} \times 40 \text{ km}$  domain will be the largest possible domain. However, this limitation in the domain extent is unlikely to be an issue for many impact studies, if we refer, for instance, to the domain sizes used in past studies that required high spatial and temporal resolution of climate inputs [e.g., Coulthard and Skinner, 2016; Paschalis *et al.*, 2014; Peleg *et al.*, 2015a].

Another potential limitation of AWE-GEN-2d is its application in areas with limited data. Some of the climate variables (e.g., cloud cover and advection) can be estimated using data derived from reanalysis products. However, the temporal and spatial resolutions obtained from the reanalysis products are too coarse to train AWE-GEN-2d for other key climate variables, such as precipitation and temperature. Two alternatives can be suggested for the calibration of AWE-GEN-2d for poorly gauged areas: (i) training AWE-GEN-2d based on data from a different location but with a similar climate and topography and (ii) training AWE-GEN-2d based on data from a high-resolution climate model output.

AWE-GEN-2d can be further developed in the future as new data products and observations will be available to refine some of the components (e.g., the representation of the near-surface wind). Additionally, AWE-GEN-2d can be used in the framework of climate change studies once appropriate methods are derived to perturb observed climate statistics with statistics simulated by climate models and use those to estimate new parameters sets. This is conceptually similar to what has been already done for the original AWE-GEN [Fatichi *et al.*, 2011, 2013; Kim and Ivanov, 2015; Fatichi *et al.*, 2016; Kim *et al.*, 2016] but will require information about changes in spatial statistics, especially for precipitation. In this regard, using regional climate models and high-resolution convective-resolving climate models [e.g., Ban *et al.*, 2014] will be likely needed to address the challenge. The main advantage of training AWE-GEN-2d to simulate future climate ensembles based on climate model data would be in its ability to simulate high-resolution climate variables in a much faster way than the original climate models do. Cross correlation among changes in climate variables and the expected inability to reparameterize all model parameters based on climate model only will rise new challenges that will be examined and discussed in future work.

## 6. Summary

AWE-GEN-2d is a new stochastic weather generator that simulates the main climatic variables (i.e., precipitation, cloud cover, air temperature, shortwave radiation, vapor pressure, relative humidity, wind speed, and atmospheric pressure) at high-temporal resolution and in a gridded format. The model is mostly an evolution and extension of two existing numerical tools AWE-GEN [Fatichi *et al.*, 2011] and STREAP [Paschalis *et al.*, 2013]. AWE-GEN-2d was calibrated and validated for the Engelberg region, an area with a complex orography located in the Swiss Alps. AWE-GEN-2d reproduces well the principal statistics for the climate variables that were simulated and analyzed across a range of spatial and temporal scales. Most important, AWE-GEN-2d has the capability to reproduce the natural variability of these climatic variables. Such a feature is fundamental for stochastic analyses aimed at investigating the role of climate variability and uncertainty of climatic forcing in impact studies in hydrology, ecology, geomorphology, and agriculture. AWE-GEN-2d is parsimonious in terms of computational demand and can be run on a high-end desktop computer, without the needs of accessing computational centers. It allows computations of multiple realizations for a given stationary climate with reduced demands of computational time in comparison to existing



climate models, thus suggesting an appealing solution for a set of problems, where natural (stochastic) climate variability cannot be neglected.

## 7. Code Availability

The MATLAB source code of AWE-GEN-2d and the data used for the Engelberg case study are available upon request from the corresponding author. The code was tested on a 64 bit high-end desktop computer with 20 threads and 128 GB of memory. Installation and compatibility of AWE-GEN-2d was verified for MATLAB versions 8.6 and 9. Any element of AWE-GEN-2d is free to use, modify, copy or distribute provided it is for academic use and source code developers are properly acknowledged and cited.

## Acknowledgments

This project is funded by the Swiss Competence Center for Energy Research-Supply of Electricity (<http://www.sccer-soe.ch>). We thank MeteoSwiss, the Swiss Federal Office of Meteorology and Climatology, for supplying climate data from ground stations and gridded products, the Swiss Federal Statistical Office for supplying the land use map (based on the *Arealstatistik 2004*) and the Swiss Federal Office of Topography for supplying the digital elevation model. We also thank the relevant PIs and their staff for establishing and maintaining the AERONET sites used in this study and the Global Modeling and Assimilation Office (GMAO) and the GES DISC for the dissemination of MERRA products. We thank the reviewers (Ethan Gutmann and an anonymous reviewer) and the Editor Paul Dirmeyer for their suggestions that considerably improved the quality of the article.

## References

- Ban, N., J. Schmidli, and C. Schär (2014), Evaluation of the convection-resolving regional climate modeling approach in decade-long simulations, *J. Geophys. Res. Atmos.*, 119, 7889–7907, doi:10.1002/2014JD021478.
- Bardossy, A., and E. J. Plate (1992), Space-time model for daily rainfall using atmospheric circulation patterns, *Water Resour. Res.*, 28(5), 1247–1259, doi:10.1029/91WR02589.
- Bell, T. (1987), A space-time stochastic model of rainfall for satellite remote-sensing studies, *J. Geophys. Res.*, 92(D8), 9631–9643, doi:10.1029/JD092iD08p09631.
- Bonan, G. (2002), *Ecological Climatology: Concept and Applications*, Cambridge Univ. Press, New York.
- Bovard, B. D., P. S. Curtis, C. S. Vogel, H.-B. Su, and H. P. Schmid (2005), Environmental controls on sap flow in a northern hardwood forest, *Tree Physiol.*, 25, 31–38, doi:10.1093/treephys/25.1.31.
- Box, G., and M. Jenkins (1970), *Time Series Analysis, Forecasting and Control*, Holden-Day, San Francisco, Calif.
- Box, G. E. P., G. M. Jenkins, and G. C. Reinsel (2008), *Linear Stationary Models*, pp. 47–91, John Wiley, Hoboken, N. J., doi:10.1002/9781118619193.ch3.
- Bracewell, R. (2000), *The Fourier Transform and Its Applications*, 3rd ed., McGraw-Hill, San Francisco, Calif.
- Burlando, M., L. Carassale, E. Georgieva, C. F. Ratto, and G. Solari (2007), A simple and efficient procedure for the numerical simulation of wind fields in complex terrain, *Boundary Layer Meteorol.*, 125(3), 417–439, doi:10.1007/s10546-007-9196-3.
- Caracciolo, D., L. V. Noto, E. Istanbuloglu, S. Fatichi, and X. Zhou (2014), Climate change and ecotone boundaries: Insights from a cellular automata ecohydrology model in a mediterranean catchment with topography controlled vegetation patterns, *Adv. Water Resour.*, 73, 159–175, doi:10.1016/j.advwatres.2014.08.001.
- Chaiwiwatworakul, P., and S. Chirattananon (2004), An investigation of atmospheric turbidity of Thai sky, *Energy Buildings*, 36, 650–659, doi:10.1016/j.enbuild.2004.01.032.
- Chambers, M. (1995), The simulation of random vector time series with given spectrum, *Math. Comput. Modell.*, 22(2), 1–6.
- Chen, Y., A. Hall, and K. N. Liou (2006), Application of three-dimensional solar radiative transfer to mountains, *J. Geophys. Res.*, 111, D21111, doi:10.1029/2006JD007163.
- Chorti, A., and D. Hristopulos (2008), Nonparametric identification of anisotropic (elliptic) correlations in spatially distributed data sets, *IEEE Trans. Signal Process.*, 56(10), 4738–4751, doi:10.1109/TSP.2008.924144.
- Chung, U., H. Seo, K. Hwang, B. Hwang, J. Choi, J. Lee, and J. Yun (2006), Minimum temperature mapping over complex terrain by estimating cold air accumulation potential, *Agric. For. Meteorol.*, 137(12), 15–24, doi:10.1016/j.agrformet.2005.12.011.
- Collins, D. B. G., R. L. Bras, and G. E. Tucker (2004), Modeling the effects of vegetation-erosion coupling on landscape evolution, *J. Geophys. Res.*, 109, F03004, doi:10.1029/2003JF000028.
- Coulthard, T. J., and C. J. Skinner (2016), The sensitivity of landscape evolution models to spatial and temporal rainfall resolution, *Earth Surf. Dyn.*, 4(3), 757–771, doi:10.5194/esurf-4-757-2016.
- Curtis, D. C., and P. S. Eagleson (1982), Constrained stochastic climate simulation, Tech. Rep. 274, Mass. Inst. of Technol. Dep. of Civ. and Environ. Eng. Ralph M. Parsons Lab., Cambridge, Mass.
- Dai, A., K. E. Trenberth, and T. R. Karl (1999), Effects of clouds, soil moisture, precipitation, and water vapor on diurnal temperature range, *J. Clim.*, 12(8), 2451–2473, doi:10.1175/1520-0442(1999)012<2451:EOCSMP>2.0.CO;2.
- Demarta, S., and A. J. McNeil (2007), The t Copula and related copulas, *Int. Stat. Rev.*, 73(1), 111–129, doi:10.1111/j.1751-5823.2005.tb00254.x.
- Deser, C., A. Phillips, V. Bourdette, and H. Teng (2012), Uncertainty in climate change projections: The role of internal variability, *Clim. Dyn.*, 38(3), 527–546, doi:10.1007/s00382-010-0977-x.
- Dingman, S. L. (1994), *Physical Hydrology*, Prentice Hall, Long Grove, Ill.
- Dozier, J., and J. Frew (1990), Rapid calculation of terrain parameters for radiation modeling from digital elevation data, *IEEE Trans. Geosci. Remote Sens.*, 28, 963–969, doi:10.1109/36.58986.
- Dubayah, R., and S. Loechel (1997), Modeling topographic solar radiation using GOES data, *J. Appl. Meteorol.*, 36, 141–154, doi:10.1175/1520-0450(1997)036<0141:MTSRUG>2.0.CO;2.
- Dubrovský, M., J. Buchtele, and Z. Žalud (2004), High-frequency and low-frequency variability in stochastic daily weather generator and its effect on agricultural and hydrologic modelling, *Clim. Change*, 63, 145–179, doi:10.1023/B:CLIM.0000018504.99914.60.
- Eagleson, P. S. (2002), *Ecohydrology: Darwinian Expression of Vegetation Form and Function*, Cambridge Univ. Press, Cambridge, U. K.
- Embrechts, P., C. Klüppelberg, and T. Mikosch (1997), *Modelling Extremal Events: For Insurance and Finance*, Springer, New York.
- Entekhabi, D., I. Rodriguez-Iturbe, and P. S. Eagleson (1989), Probabilistic representation of the temporal rainfall process by a modified Neyman-Scott rectangular pulses model: Parameter estimation and validation, *Water Resour. Res.*, 25(2), 295–302, doi:10.1029/WR025i002p00295.
- Fatichi, S., and V. Y. Ivanov (2014), Interannual variability of evapotranspiration and vegetation productivity, *Water Resour. Res.*, 50, 3275–3294, doi:10.1002/2013WR015044.
- Fatichi, S., V. Y. Ivanov, and E. Caporali (2011), Simulation of future climate scenarios with a weather generator, *Adv. Water Resour.*, 34(4), 448–467, doi:10.1016/j.advwatres.2010.12.013.
- Fatichi, S., V. Y. Ivanov, and E. Caporali (2013), Assessment of a stochastic downscaling methodology in generating an ensemble of hourly future climate time series, *Clim. Dyn.*, 40(7), 1841–1861, doi:10.1007/s00382-012-1627-2.

- Fatichi, S., S. Rimkus, P. Burlando, R. Bordoy, and P. Molnar (2015), High-resolution distributed analysis of climate and anthropogenic changes on the hydrology of an alpine catchment, *J. Hydrol.*, 525, 362–382, doi:10.1016/j.jhydrol.2015.03.036.
- Fatichi, S., V. Y. Ivanov, A. Paschalis, N. Peleg, P. Molnar, S. Rimkus, J. Kim, P. Burlando, and E. Caporali (2016), Uncertainty partition challenges the predictability of vital details of climate change, *Earth's Future*, 4(5), 240–251, doi:10.1002/2015EF000336.
- Fowler, H. J., C. G. Kilsby, and P. E. O'Connel (2000), A stochastic rainfall model for the assessment of regional water resource systems under changed climatic conditions, *Hydrol. Earth Syst. Sci.*, 4(2), 263–282, doi:10.5194/hess-4-263-2000.
- Fowler, H. J., S. Blenkinsop, and C. Tebaldi (2007), Linking climate change modelling to impacts studies: Recent advances in downscaling techniques for hydrological modelling, *Int. J. Climatol.*, 27, 1547–1578, doi:10.1002/joc.1556.
- Furrer, E. M., and R. W. Katz (2008), Improving the simulation of extreme precipitation events by stochastic weather generators, *Water Resour. Res.*, 44, W12439, doi:10.1029/2008WR007316.
- Francipane, A., S. Fatichi, V. Y. Ivanov, and L. V. Noto (2015), Stochastic assessment of climate impacts on hydrology and geomorphology of semiarid headwater basins using a physically based model, *J. Geophys. Res. Earth Surf.*, 120, 507–533, doi:10.1002/2014JF003232.
- Frei, C. (2014), Interpolation of temperature in a mountainous region using nonlinear profiles and non-Euclidean distances, *Int. J. Climatol.*, 34(5), 1585–1605, doi:10.1002/joc.3786.
- Frei, C., and C. Schär (1998), A precipitation climatology of the Alps from high-resolution rain-gauge observations, *Int. J. Climatol.*, 18(8), 873–900, doi:10.1002/(SICI)1097-0088(19980630)18:8<873::AID-JOC255>3.0.CO;2-9.
- Frigo, M., and S. G. Johnson (1998), FFTW: An adaptive software architecture for the FFT, *Acoust. Speech Signal Process.*, 3, 1381–1384, doi:10.1109/ICASSP.1998.681704.
- Gabella, M., M. Bolliger, U. Germann, and G. Perona (2005), Large sample evaluation of cumulative rainfall amounts in the alps using a network of three radars, *Atmos. Res.*, 77(14), 256–268, doi:10.1016/j.atmosres.2004.10.014.
- Gabriel, K. R., and J. Neumann (1962), A Markov chain model for daily rainfall occurrence at Tel Aviv, *Q. J. R. Meteorol. Soc.*, 88(375), 90–95, doi:10.1002/qj.49708837511.
- Georgieva, E., E. Canepa, A. Mazzino, and C. Ratto (2003), *Winds Release 4.2 User Guide*, Dep. of Phys., Univ. of Genova, Genova, Italy.
- Germann, U., G. Galli, M. Boschetti, and M. Bolliger (2006), Radar precipitation measurement in a mountainous region, *Q. J. R. Meteorol. Soc.*, 132(618), 1669–1692, doi:10.1256/qj.05.190.
- Gneiting, T. (2010), Matérn cross-covariance functions for multivariate random fields, *J. Am. Stat. Assoc.*, 105(491), 1167–1177, doi:10.1198/jasa.2010.tm09420.
- Gueymard, C. A. (1989), A two-band model for the calculation of clear sky solar irradiance, illuminance, and photosynthetically active radiation at the earth's surface, *Solar Energy*, 43, 253–265, doi:10.1016/0038-092X(89)90113-8.
- Gueymard, C. A. (2003), Direct solar transmittance and irradiance predictions with broadband models: Part 1: Detailed theoretical performance assessment, *Solar Energy*, 74, 355–379, doi:10.1016/S0038-092X(03)00195-6.
- Gueymard, C. A. (2004), Corrigendum to "Direct solar transmittance and irradiance predictions with broadband models: Part 1: Detailed theoretical performance assessment," *Solar Energy*, 76, 513.
- Gueymard, C. A. (2008), REST2: High-performance solar radiation model for cloudless-sky irradiance illuminance and photosynthetically active radiation—Validation with a benchmark dataset, *Solar Energy*, 82, 272–285, doi:10.1016/j.solener.2007.04.008.
- Guillot, G. (1999), Approximation of Sahelian rainfall fields with meta-Gaussian random functions, *Stochastic Environ. Res. Risk Assess.*, 13(1–2), 100–112, doi:10.1007/s004770050034.
- Gutmann, E., I. Barstad, M. Clark, J. Arnold, and R. Rasmussen (2016), The intermediate complexity atmospheric research model (ICAR), *J. Hydrometeorol.*, 17(3), 957–973, doi:10.1175/JHM-D-15-0155.1.
- Gutnisky, D. A., and K. Josić (2010), Generation of spatiotemporally correlated spike trains and local field potentials using a multivariate autoregressive process, *J. Neurophysiol.*, 103(5), 2912–30, doi:10.1152/jn.00518.2009.
- Haberlandt, U., A.-D. Ebner von Eschenbach, and I. Buchwald (2008), A space-time hybrid hourly rainfall model for derived flood frequency analysis, *Hydrol. Earth Syst. Sci.*, 12(6), 1353–1367, doi:10.5194/hess-12-1353-2008.
- Hammer, A., D. Heinemann, C. Hoyer, R. Kuhlemann, E. Lorenz, R. Müller, and H. G. Beyer (2003), Solar energy assessment using remote sensing technologies, *Remote Sens. Environ.*, 86(3), 423–432, doi:10.1016/S0034-4257(03)00083-X.
- Hansen, J. W., and T. Mavromatis (2001), Correcting low-frequency variability bias in stochastic weather generators, *Agric. For. Meteorol.*, 109, 297–310, doi:10.1016/S0168-1923(01)00271-4.
- Hayhoe, H. N. (2000), Improvements of stochastic weather data generators for diverse climates, *Clim. Res.*, 14(2), 75–87, doi:10.3354/cr014075.
- Hoffmann, H., et al. (2015), Variability of effects of spatial climate data aggregation on regional yield simulation by crop models, *Clim. Res.*, 65, 53–69, doi:10.3354/cr01326.[10.3354/cr01326]
- Holben, B. N., et al. (2001), An emerging ground-based aerosol climatology: Aerosol optical depth from aaronet, *J. Geophys. Res.*, 106(D11), 12,067–12,097, doi:10.1029/2001JD900014.
- Hutchinson, M. F. (1995), Stochastic space-time weather models from ground-based data, *Agric. For. Meteorol.*, 73(3), 237–264, doi:10.1016/0168-1923(94)05077-J.
- Ingold, T., C. Mätzler, N. Kämpfer, and A. Heimo (2001), Aerosol optical depth measurements by means of a sun photometer network in Switzerland, *J. Geophys. Res.*, 106(D21), 27,537–27,554, doi:10.1029/2000JD000088.
- Iqbal, M. (1983), *An Introduction to Solar Radiation*, Academic, Toronto, Canada.
- Ivanov, V. Y., R. L. Bras, and D. C. Curtis (2007), A weather generator for hydrological, ecological, and agricultural applications, *Water Resour. Res.*, 43, W10406, doi:10.1029/2006WR005364.
- Johnson, N. L. (1949), Systems of frequency curves generated by methods of translation, *Biometrika*, 36(1/2), 149–176, doi:10.2307/2332539.
- Jones, P. D., C. G. Kilsby, C. Harpham, V. Glenis, and A. Burton (2009), *UK Climate Projections Science Report: Projections of Future Daily Climate for the UK From the Weather Generator*, Met Office, Exeter, U. K.
- Jones, P. G., and P. K. Thornton (2000), Marksim: Software to generate daily weather data for Latin America and Africa, *Agron. J.*, 92(3), 445–453, doi:10.2134/agronj2000.923445x.
- Kasten, F., and G. Czeplak (1980), Solar and terrestrial radiation dependent on the amount and type of cloud, *Solar Energy*, 24, 177–189, doi:10.1016/0038-092X(80)90391-6.
- Katz, R. W., and M. B. Parlange (1998), Overdispersion phenomenon in stochastic modeling of precipitation, *J. Clim.*, 11(4), 591–601, doi:10.1175/1520-0442(1998)011<0591:OPISMO>2.0.CO;2.
- Kerr, R. A. (2011), Vital details of global warming are eluding forecasters, *Science*, 334(6053), 173–174, doi:10.1126/science.334.6053.173.
- Kim, J., and V. Y. Ivanov (2015), A holistic, multi-scale dynamic downscaling framework for climate impact assessments and challenges of addressing finer-scale watershed dynamics, *J. Hydrol.*, 522, 645–660, doi:10.1016/j.jhydrol.2015.01.025.

- Kim, J., V. Y. Ivanov, and S. Fatichi (2016), Climate change and uncertainty assessment over a hydroclimatic transect of Michigan, *Stochastic Environ. Res. Risk Assess.*, 30(3), 923–944, doi:10.1007/s00477-015-1097-2.
- Kleiber, W., R. W. Katz, and B. Rajagopalan (2012), Daily spatiotemporal precipitation simulation using latent and transformed Gaussian processes, *Water Resour. Res.*, 48, W01523, doi:10.1029/2011WR011105.
- Kopp, G., and J. L. Lean (2011), A new, lower value of total solar irradiance: Evidence and climate significance, *Geophys. Res. Lett.*, 38, L01706, doi:10.1029/2010GL045777.
- Kundu, P. K., and T. Bell (2003), A stochastic model of space-time variability of mesoscale rainfall: Statistics of spatial averages, *Water Resour. Res.*, 39(12), 1328, doi:10.1029/2002WR001802.
- Kyznarov, H., and P. Novk (2009), CELLTRACK—Convective cell tracking algorithm and its use for deriving life cycle characteristics, *Atmos. Res.*, 93(13), 317–327, doi:10.1016/j.atmosres.2008.09.019.
- Lalas, D. (1985), Wind energy estimation and siting in complex terrain, *Int. J. Solar Energy*, 3(2), 43–71, doi:10.1080/01425918508914383.
- Lalas, D., M. Tombrou, and M. Petrakis (1988), Comparison of the performance of some numerical wind energy siting codes in rough terrain, in *European Community Wind Energy Conference*, pp. 110–114, Commission of the European Communities, Luxembourg.
- Lang, A., and J. Potthoff (2011), Fast simulation of Gaussian random fields, *Monte Carlo Methods Appl.*, 17(3), 195–214, doi:10.1515/mcma.2011.009.
- LeCam, L. (1961), A stochastic description of precipitation, in *Proceedings of Fourth Berkeley Symposium on Mathematical Statistics and Probability*, vol. 3, edited by J. Neyman, pp. 165–176, Univ. of Calif. Press, Berkeley.
- Li, L., W. Schmid, and J. Joss (1995), Nowcasting of motion and growth of precipitation with radar over a complex orography, *J. Appl. Meteorol.*, 34(6), 1286–1300, doi:10.1175/1520-0450(1995)034<1286:NOMAGO>2.0.CO;2.
- Liston, G. E., and K. Elder (2006), A meteorological distribution system for high-resolution terrestrial modeling (micromet), *J. Hydrometeorol.*, 7(2), 217–234, doi:10.1175/JHM486.1.
- Liston, G. E., and M. Sturm (1998), A snow-transport model for complex terrain, *J. Glaciol.*, 44(148), 498–516, doi:10.3198/1998JoG44-148-498-516.
- Liu, C. V., and W. R. Goodin (1976), An iterative algorithm for objective wind field analysis, *Mon. Weather Rev.*, 104(6), 784–792, doi:10.1175/1520-0493(1976)104<0784:AIAFOW>2.0.CO;2.
- Lütkepohl, H. (2005), *New Introduction to Multiple Time Series Analysis*, Springer Sci. and Bus. Media, Berlin, Heidelberg.
- Marty, C., R. Philippon, C. Fröhlich, and A. Ohmura (2002), Altitude dependence of surface radiation fluxes and cloud forcing in the alps: Results from the alpine surface radiation budget network, *Theor. Appl. Climatol.*, 72(3), 137–155, doi:10.1007/s007040200019.
- Mavromatis, T., and J. W. Hansen (2001), Interannual variability characteristics and simulated crop response of four stochastic weather generators, *Agric. For. Meteorol.*, 109, 283–296, doi:10.1016/S0168-1923(01)00272-6.
- McKague, K., R. Rudra, and J. Ogilvie (2003), CLIMGEN—A convenient weather generator tool for Canadian climate stations, paper presented at the Meeting of the CSAE/SCGR Canadian Society for Engineering in Agricultural Food and Biological Systems, Montreal, Quebec, Canada, 6–9 July.
- MeteoSwiss (2016), *Daily Precipitation (Final Analysis): RhiresD*, Switzerland. [Available at <http://www.meteoswiss.admin.ch/home/search.subpage.html/en/data/products/2014/raeumliche-daten-niederschlag.html>.]
- Minville, M., F. Brissette, and R. Leconte (2010), Impacts and uncertainty of climate change on water resource management of the Peribonka River System (Canada), *J. Water Resour. Plann. Manage.*, 136(3), 376–385, doi:10.1061/(ASCE)WR.1943-5452.0000041.
- Mohan, M., and T. Siddiqui (1998), Analysis of various schemes for the estimation of atmospheric stability classification, *Atmos. Environ.*, 32(21), 3775–3781, doi:10.1016/S1352-2310(98)00109-5.
- Morgan, E. C., M. Lackner, R. M. Vogel, and L. G. Baise (2011), Probability distributions for offshore wind speeds, *Energy Convers. Manage.*, 52(1), 15–26, doi:10.1016/j.enconman.2010.06.015.
- Neumaier, A., and T. Schneider (2001), Estimation of parameters and eigenmodes of multivariate autoregressive models, *ACM Trans. Math. Software*, 27(1), 27–57, doi:10.1145/382043.382304.
- Nicks, A. D., L. J. Lane, and G. A. Gander (1995), Weather generator, in *USDA-Water Erosion Prediction Project: Hillslope Profile and Watershed Model Documentation*, chap. 2, pp. 1–22, USDA-ARS Natl. Soil Erosion Res. Lab., West Lafayette, Ind.
- Niemi, T. J., J. H. A. Guillaume, T. Kokkonen, T. M. T. Hoang, and A. W. Seed (2016), Role of spatial anisotropy in design storm generation: Experiment and interpretation, *Water Resour. Res.*, 52, 69–89, doi:10.1002/2015WR017521.
- Ochoa-Rodriguez, S., et al. (2015), Impact of spatial and temporal resolution of rainfall inputs on urban hydrodynamic modelling outputs: A multi-catchment investigation, *J. Hydrol.*, 531(2, SI), 389–407, doi:10.1016/j.jhydrol.2015.05.035.
- Olseth, J. A., and A. Skartveit (1997), Spatial distribution of photosynthetically active radiation over complex topography, *Agric. For. Meteorol.*, 86, 205–214, doi:10.1016/S0168-1923(97)00010-5.
- Olseth, J. A., A. Skartveit, and H. Zou (1995), Spatially continuous mapping of solar resources in a complex high latitude topography, *Solar Energy*, 55(6), 475–485, doi:10.1016/0038-092X(95)00068-3.
- Papoulis, A., and S. Unnikrishna (2002), *Probability, Random Variables and Stochastic Processes*, 4th ed., McGraw-Hill, New York, N. Y.
- Park, J. Y., and S. J. Kim (2014), Potential impacts of climate change on the reliability of water and hydropower supply from a multipurpose dam in South Korea, *J. Am. Water Resour. Assoc.*, 50(5), 1273–1288, doi:10.1111/jawr.12190.
- Parlange, M. B., and R. W. Katz (2000), An extended version of the Richardson model for simulating daily weather variables, *J. Appl. Meteorol.*, 39, 610–622, doi:10.1175/1520-0450-39.5.610.
- Paschalis, A. (2013), Modelling the space-time structure of precipitation and its impact on basin response, PhD thesis, Diss., Eidg. Tech. Hochschule, ETH Zürich, Zürich, Switzerland.
- Paschalis, A., P. Molnar, S. Fatichi, and P. Burlando (2013), A stochastic model for high-resolution space-time precipitation simulation, *Water Resour. Res.*, 49, 8400–8417, doi:10.1002/2013WR014437.
- Paschalis, A., S. Fatichi, P. Molnar, S. Rimkus, and P. Burlando (2014), On the effects of small scale spacetime variability of rainfall on basin flood response, *J. Hydrol.*, 514, 313–327, doi:10.1016/j.jhydrol.2014.04.014.
- Pasquill, F. (1974), *Atmospheric Diffusion*, Halsted, New York.
- Pegram, G. G., and A. N. Clothier (2001a), High resolution space-time modelling of rainfall: The “String of Beads” model, *J. Hydrol.*, 241, 26–41, doi:10.1016/S0022-1694(00)00373-5.
- Pegram, G. G., and A. N. Clothier (2001b), Downscaling rainfields in space and time, using the String of Beads model in time series mode, *Hydrol. Earth Syst. Sci.*, 5(2), 175–186, doi:10.5194/hess-5-175-2001.
- Peleg, N., and E. Morin (2012), Convective rain cells: Radar-derived spatiotemporal characteristics and synoptic patterns over the eastern Mediterranean, *J. Geophys. Res.*, 117, D15116, doi:10.1029/2011JD017353.
- Peleg, N., and E. Morin (2014), Stochastic convective rain-field simulation using a high-resolution synoptically conditioned weather generator (HiReS-WG), *Water Resour. Res.*, 50, 2124–2139, doi:10.1002/2013WR014836.

- Peleg, N., E. Shamir, K. P. Georgakakos, and E. Morin (2015a), A framework for assessing hydrological regime sensitivity to climate change in a convective rainfall environment: A case study of two medium-sized eastern Mediterranean catchments, Israel, *Hydrol. Earth Syst. Sci.*, 19(1), 567–581, doi:10.5194/hess-19-567-2015.
- Peleg, N., F. Blumensaat, S. Fatichi, P. Paschalis, P. Molnar, and P. Burlando (2015b), High-resolution stochastic generation of rainfall for urban hydrological applications, in *UrbanRain15: 10th International Workshop on Precipitation in Urban Areas, 1–5 December 2015, Sporthotel Pontresina, Switzerland*, edited by P. Molnar and N. Peleg, pp. UR15–UR57, ETH Zürich, Zürich, Switzerland, doi:10.3929/ethz-a-010549004.
- Peleg, N., F. Marra, S. Fatichi, A. Paschalis, P. Molnar, and P. Burlando (2016), Spatial variability of extreme rainfall at radar subpixel scale, *J. Hydrol.*, doi:10.1016/j.jhydrol.2016.05.033.
- Peleg, N., F. Blumensaat, P. Molnar, S. Fatichi, and P. Burlando (2017), Partitioning the impacts of spatial and climatological rainfall variability in urban drainage modeling, *Hydrol. Earth Syst. Sci.*, 21, 1559–1572, doi:10.5194/hess-21-1559-2017.
- Phillips, G. T. (1979), Preliminary user's guide for the NOABL objective analysis code. Special report, 15 June 1977–15 June 1978, *Rep. DOE/ET/20280-T1*, Sci. Appl., Inc., La Jolla, Calif., doi:10.2172/7080538.
- Pickering, N., J. W. Hansen, J. Jones, C. Wells, V. Chan, and D. Godwin (1994), Weatherman: A utility for managing and generating daily weather data, *Agron. J.*, 86(2), 332–337, doi:10.2134/agronj1994.00021962008600020023x.
- Prein, A. F., et al. (2015), A review on regional convection-permitting climate modeling: Demonstrations, prospects, and challenges, *Rev. Geophys.*, 53(2), 323–361, doi:10.1002/2014RG000475.
- Price, M. F., A. C. Byers, D. A. Friend, T. Kohler, and L. W. Price (2013), *Mountain Geography: Physical and Human Dimensions*, Univ. of Calif. Press, Oakland, Calif.
- Qian, B., S. Gameda, H. Hayhoe, R. De Jong, and A. Bootsma (2004), Comparison of LARS-WG and AAFC-WG stochastic weather generators for diverse Canadian climates, *Clim. Res.*, 26(3), 175–191, doi:10.3354/cr026175.
- Racsko, P., L. Szeidl, and M. Semenov (1991), A serial approach to local stochastic weather models, *Ecol. Modell.*, 57(1), 27–41, doi:10.1016/0304-3800(91)90053-4.
- Ramanathan, V., P. J. Crutzen, J. T. Kiehl, and D. Rosenfeld (2001), Aerosols, climate, and the hydrological cycle, *Science*, 294(5549), 2119–2124, doi:10.1126/science.1064034.
- Ratto, C., R. Festa, O. Nicora, R. Mosiello, A. Ricci, D. Lalas, and O. Frumento (1990), Wind field numerical simulations: A new user-friendly code, in *1990 European Community Wind Energy Conference*, pp. 10–14, H.S. Stephens, Bedford, U. K.
- Ratto, C., R. Festa, C. Romeo, O. Frumento, and M. Galluzzi (1994), Mass-consistent models for wind fields over complex terrain: The state of the art, *Environ. Software*, 9(4), 247–268, doi:10.1016/0266-9838(94)90023-X.
- Richardson, C. W. (1981), Stochastic simulation of daily precipitation, temperature, and solar radiation, *Water Resour. Res.*, 17(1), 182–190, doi:10.1029/WR017i001p00182.
- Richardson, C. W., and D. A. Wright (1984), WGEN: A model for generating daily weather variables, *Rep. ARS 8*, U.S. Dep. of Agric., Agric. Res. Serv., Washington, D. C.
- Rienecker, M. M., et al. (2011), Merra: Nasas modern-era retrospective analysis for research and applications, *J. Clim.*, 24(14), 3624–3648, doi:10.1175/JCLI-D-11-00015.1.
- Roberts, J. S. (2010), Dew point temperature, in *Encyclopedia of Agricultural, Food, and Biological Engineering*, edited by D. R. Heldman and C. I. Moraru, chap. 73, pp. 286–291, CRC Press, Boca Raton, Fla, doi:10.1081/E-EAFE2-120045576.
- Robertson, A., J. Overpeck, D. Rind, E. Mosley-Thompson, G. Zielinski, J. Lean, D. Koch, J. Penner, I. Tegen, and R. Healy (2001), Hypothesized climate forcing time series for the last 500 years, *J. Geophys. Res.*, 106(D14), 14,783–14,803, doi:10.1029/2000JD900469.
- Rockel, B., A. Will, and A. Hense (2008), The regional climate model COSMO-CLM (CCLM), *Meteorol. Z.*, 17(4), 347–348, doi:10.1127/0941-2948/2008/0309.
- Russell, P. B., et al. (2002), Comparison of aerosol single scattering albedos derived by diverse techniques in two North Atlantic experiments, *J. Atmos. Sci.*, 59, 609–619, doi:10.1175/1520-0469(2002)059<0609:COASSA>2.0.CO;2.
- Schlabing, D., M. Frassl, M. Eder, K. Rinke, and A. Brdossy (2014), Use of a weather generator for simulating climate change effects on ecosystems: A case study on Lake Constance, *Environ. Modell. Software*, 61, 326–338, doi:10.1016/j.envsoft.2014.06.028.
- Schleiss, M., J. Jaffrain, and A. Berne (2012), Stochastic simulation of intermittent DSD fields in time, *J. Hydrometeorol.*, 13(2), 621–637, doi:10.1175/JHM-D-11-018.1.
- Schleiss, M. A., A. Berne, and R. Uijlenhoet (2009), Geostatistical simulation of two-dimensional fields of raindrop size distributions at the meso-gamma scale, *Water Resour. Res.*, 45, W07415, doi:10.1029/2008WR007545.
- Schneider, T., and A. Neumaier (2001), Algorithm 808: ARfit—A matlab package for the estimation of parameters and eigenmodes of multivariate autoregressive models, *ACM Trans. Math. Software*, 27(1), 58–65, doi:10.1145/382043.382316.
- Schuol, J., and K. Abbaspour (2007), Using monthly weather statistics to generate daily data in a SWAT model application to West Africa, *Ecol. Modell.*, 201(34), 301–311, doi:10.1016/j.ecolmodel.2006.09.028.
- Schwarb, M. (2000), The alpine precipitation climate: Evaluation of a high-resolution analysis scheme using comprehensive rain-gauge data, PhD thesis, dissertation, 131 pp., Swiss Fed. Inst. of Technol., Zürich, Switzerland.
- Semenov, M. A. (2006), Using weather generators in crop modelling, in *Acta Hort.*, 707, 93–100.
- Semenov, M. A., and E. M. Barrow (1997), Use of a stochastic weather generator in the development of climate change scenarios, *Clim. Change*, 35, 397–414, doi:10.1023/A:1005342632279.
- Semenov, M. A., and E. M. Barrow (2002), *LARS-WG, A Stochastic Weather Generator for Use in Climate Impact Studies, Version 3.0*. [Available at <http://resources.rothamsted.ac.uk/sites/default/files/groups/mas-models/download/LARS-WG-Manual.pdf>]
- Semenov, M. A., and J. R. Porter (1995), Climatic variability and the modelling of crop yields, *Agric. For. Meteorol.*, 73, 265–283, doi:10.1016/0168-1923(94)05078-K.
- Sharples, A. N., and J. R. Williams (1990), EPIC-erosion/productivity impact calculator: 1. Model documentation, *Tech. Bull.* 1768, 235 pp., U.S. Dep. of Agric., Washington, D. C.
- Skamarock, W. C., J. B. Klemp, J. Dudhia, D. O. Gill, D. M. Barker, W. Wang, and J. G. Powers (2005), A description of the advanced research WRF version 2, DTIC document, Technical report: NCAR/TN468+STR, NCAR Technical note, National Center for Atmospheric Research, Boulder, Colo.
- Slingo, A. (1989), A GCM parameterization for the shortwave radiative properties of water clouds, *J. Atmos. Sci.*, 46(10), 1419–1427, doi:10.1175/1520-0469(1989)046<1419:AGPFTS>2.0.CO;2.
- Stephens, G. L. (1978), Radiation profiles in extended water clouds: 2. Parameterization schemes, *J. Atmos. Sci.*, 35(11), 2123–2132, doi:10.1175/1520-0469(1978)035<2123:RPIEWC>2.0.CO;2.
- Stöckli, R. (2013), The HelioMont surface solar radiation processing, *Sci. Rep.* 93, 119 pp., MeteoSwiss: Fed. Off. of Meteorol. and Climatol., Switzerland.



- Thompson, D. W. J., E. A. Barnes, C. Deser, W. E. Foust, and A. S. Phillips (2015), Quantifying the role of internal climate variability in future climate trends, *J. Clim.*, *28*(16), 6443–6456, doi:10.1175/JCLI-D-14-00830.1.
- Tucker, G. E., and R. L. Bras (2000), A stochastic approach to modeling the role of rainfall variability in drainage basin evolution, *Water Resour. Res.*, *36*(7), 1953–1964, doi:10.1029/2000WR900065.
- TVA (1972), Heat and mass transfer between a water surface and the atmosphere, *Tech. Rep. 14*, Tenn. Valley Auth. Water Resour. Res. Eng. Lab., Norris.
- Vrac, M., and P. Naveau (2007), Stochastic downscaling of precipitation: From dry events to heavy rainfalls, *Water Resour. Res.*, *43*, W07402, doi:10.1029/2006WR005308.
- Wetterhall, F., A. Bárdossy, D. Chen, S. Halldin, and C.-y. Xu (2008), Statistical downscaling of daily precipitation over sweden using gcm output, *Theor. Appl. Climatol.*, *96*(1), 95–103, doi:10.1007/s00704-008-0038-0.
- Wheater, H., R. Chandler, C. Onof, V. Isham, E. Bellone, C. Yang, D. Lekkas, G. Lourmas, and M.-L. Segond (2005), Spatial-temporal rainfall modelling for flood risk estimation, *Stochastic Environ. Res. Risk Assess.*, *19*, 403–416, doi:10.1007/s00477-005-0011-8.
- Whiteman, D. (1982), Breakup of temperature inversions in deep mountain valleys: Part I. Observations, *J. Appl. Meteorol.*, *21*(3), 270–289, doi:10.1175/1520-0450(1982)021<0270:BOTIID>2.0.CO;2.
- Wieringa, J. (1992), Updating the Davenport roughness classification, *J. Wind Eng. Ind. Aerodyn.*, *41*(1), 357–368, doi: 10.1016/0167-6105(92)90434-C.
- Wieringa, J. (1993), Representative roughness parameters for homogeneous terrain, *Boundary Layer Meteorol.*, *63*(4), 323–363, doi:10.1007/BF00705357.
- Wilks, D. S. (1999), Interannual variability and extreme-value characteristics of several stochastic daily precipitation models, *Agric. For. Meteorol.*, *93*, 153–169, doi:10.1016/S0168-1923(98)00125-7.
- Wilks, D. S., and R. L. Wilby (1999), The weather generation game: A review of stochastic weather models, *Prog. Phys. Geogr.*, *23*, 329–357, doi:10.1177/030913339902300302.
- Woolhiser, D. A., and J. Roldn (1982), Stochastic daily precipitation models: 2. A comparison of distributions of amounts, *Water Resour. Res.*, *18*(5), 1461–1468, doi:10.1029/WR018i005p01461.
- Zilitinkevich, S. S. (1989), Velocity profiles, the resistance law and the dissipation rate of mean flow kinetic energy in a neutrally and stably stratified planetary boundary layer, *Boundary Layer Meteorol.*, *46*(4), 367–387, doi:10.1007/BF00172242.